Chapter 10

Structures and Dynamics of Interfacial Water Assembly on a Hydrophobic Silicon Surface

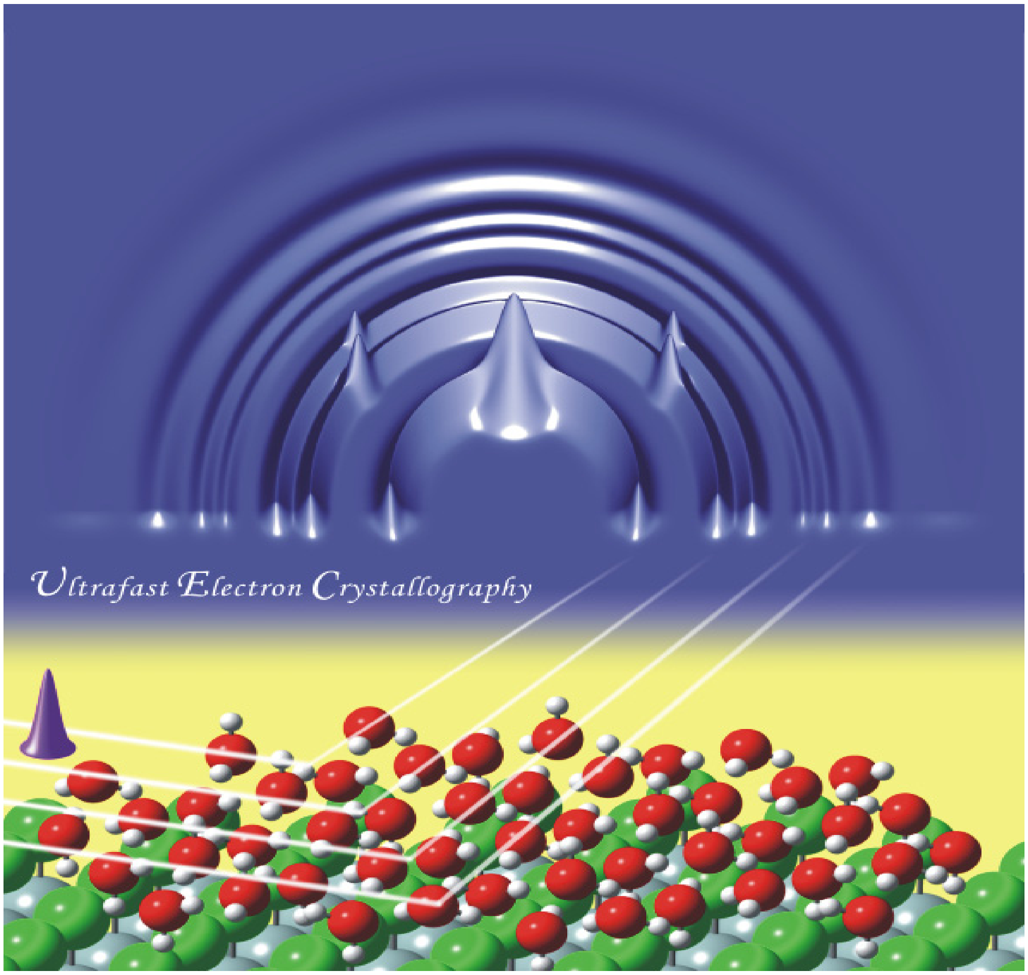

Introduction

The study of water at interfaces on the nanometer scale is of fundamental significance, principally as a result of the ubiquitous nature of hydrophobic and hydrophilic interactions throughout the physical, chemical and biological sciences (*1-3*). The understanding of various important phenomena—such as wetting (*4-6*) and hydration (*7-9*), chemical reactivity (*5, 10, 11*), molecular recognition (*12, 13*), and macromolecular folding (*14*)—eminently relies on the elucidation of the structure and dynamics of interfacial water. However, because of the polar nature of a water molecule, the directional nature of hydrogen bonding, and comparable water–substance interactions, even a further understanding of the structure of interfacial water assemblies presents several challenges (*15*). Moreover, besides the energetics, the time scales of atomic motions and structural dynamics, whether locally or collectively over a long range, are important for defining the microscopic mechanisms of relaxations, the stability and phase transformations between various water structures, and the role of substrate structure and morphology (see Ch. 9).

Structurally, interfacial water may adopt a number of different structures, ranging from amorphous solid water with only a short-range molecular order (*16*), to crystalline polymorphs which exhibit ordering of a longer range with or without the assistance from the neighboring substance. Spectroscopic techniques, such as internal reflection (*17*) and second-harmonic and sum-frequency generation (SFG) spectroscopy (*2, 18, 19*), are capable of capturing signatures of structural and surface molecular changes. For example, static SFG measurements showed the decay length of polar ordering of ice films on a Pt(111) surface to be ~30 monolayers (*20*); transient SFG response from D_2O ice on CO/Pt(111) has indicated the presence of melting and recrystallization without desorption

(*21*). However, these studies provide only indirect information about the overall structure and order of an interfacial water assembly, let alone the resolution of the motions and dynamics at atomic scale.

A recent real-space study of the formation of ice films as many as 30 molecular layers thick under the influence of the Pt(111) surface morphology was performed using scanning tunneling microscopy (*22*). In our laboratory, direct structural determination of interfacial water is achieved through reciprocal-space diffraction of electrons. When exploited in reflection geometry, electron crystallography (*23*) is ideal for surface and interface probings because of the large electron scattering cross section. With the equipment of an ultrashort temporal resolution, the technique of ultrafast electron crystallography (UEC) can provide direct knowledge of both static and transient structures of an interfacial water assembly from the diffraction images recorded, with atomic-scale spatial resolution. As demonstrated in a previous report for water on a hydrophilic substrate (*24*), the structure and dynamics of ordered water layers were found to be different from those of the bulk.

In this chapter, I focus on the properties of interfacial water deposited onto a hydrophobic substrate—the hydrogen-terminated silicon (111) surface—under the ultrahigh vacuum (UHV) condition. Structurally, without a substantial interaction with the underlying substrate (*24*) or the assistance from a morphology template (Ch. 9), the immobilized water molecules are shown to rearrange into randomly oriented crystallites of the cubic ice (*Ic*) form; a detailed structural analysis will be presented. Dynamically, after the ultrafast heating of the silicon substrate by an infrared femtosecond pulse, the interfacial ice crystallites goes through nonequilibrium phase transformation into a highly expanded lattice. This dynamical behavior is evidenced by the appearance of a “structural isosbestic point" in the diffraction profiles, which was also observed in interfacial water assemblies on graphite (Ch. 9). From the time scales involved and fluence dependence of the structural dynamics, a physical picture is reached for the dynamics and interaction between interfacial water and the underlying silicon substrate.

Materials and Experimental Section

The silicon substrate with an atomically flat hydrogen-terminated (111) surface [H/Si(111)] was prepared from a crystalline wafer (*p*-type B-doped, 0.5 mm in thickness, $\rho = 1–30\ \Omega\cdot\text{cm}$), by first cleaning and oxidizing in a standard RCA–1 solution (*25*) followed by etching in a 40 wt% NH_4F solution for 3 minutes and rinsing in deionized water for a few seconds (*26, 27*). After the surface preparation, the substrate was immediately mounted onto a goniometer in the diffraction chamber for an ultrahigh vacuum environment. In order to achieve the best thermal contact, a sheet of indium was placed underneath the sample and mechanical clips were used to secure it to the sample holder. A calibrated K-type thermocouple was directly attached to the substrate surface, using copper tape and a mechanical clip, for measurement of the sample temperature with an accuracy of ±0.5 K. The entire sample holder was readily cooled and maintained at low temperature by a controlled flow of liquid nitrogen.

At the base temperature of $T \sim 100$ K the H/Si(111) surface was dosed by water (NANOpure, resistivity > 18.0 MΩ·cm), using a capillary doser (connected on top of the diffraction chamber) containing only saturated water vapor of ~20 Torr at room temperature after repeated freeze–pump–thaw cycles; molecules of water were then effused through a micrometer-sized pinhole that was 3 cm above the substrate inside the chamber (*24*). The pressure in the diffraction chamber was in the 10^{-9}-torr range while dosing and at ~10^{-10} torr during the diffraction experiments. By controlling the dose time, different amounts of water were deposited on the substrate surface. Without the initiating T-jump laser pulse, the UEC apparatus can be used to record static (time-averaged) diffraction patterns in the reflection geometry, allowing characterization of the structure of the interfacial water assembly. Such patterns contain diffraction features that correspond to the intersections of the Ewald sphere and the reciprocal lattice defined by the sample (Ch. 2), and are characterized by the momentum transfer coordinate $s = (4\pi/\lambda)\sin(\theta/2)$ where θ is the total angle of scattering.

The time-resolved experiments were carried out after the deposited interfacial water was thermally crystallized (annealed) and then maintained at $T = 100$ K. At the excitation wavelength of 800 nm for substrate temperature jump and at the present adsorbate thickness, there is no absorption in the water layers. The electron beam had a cross section diameter of ~300 μm on the screen, and was directed onto the sample at a grazing incidence angle of typically <1° to probe nanometer-scale interfacial assemblies. No surface charging or deterioration was resulted from the electron bombardment, as evidenced by the steadiness of the unblocked (undiffracted) electron beam and the diffraction pattern that are repeatedly recorded over many hours. The electron diffraction patterns were recorded for different delay times between the optical and electron pulses. The optical excitation fluence used was up to 90 mJ/cm^2 at the peak. Because of the capillary doser above the chamber, the scheme of pulse front tilting that enables femtosecond resolution (*28*) was not employed, but the temporal resolution (capable of detecting 2-ps change; 7 ps in total) was sufficient for the dynamics. The ice–substrate composite was fully recovered in less than 1 ms without noticeable water sublimation, as evidenced by the reproducibility of the diffraction pattern at negative times and for our

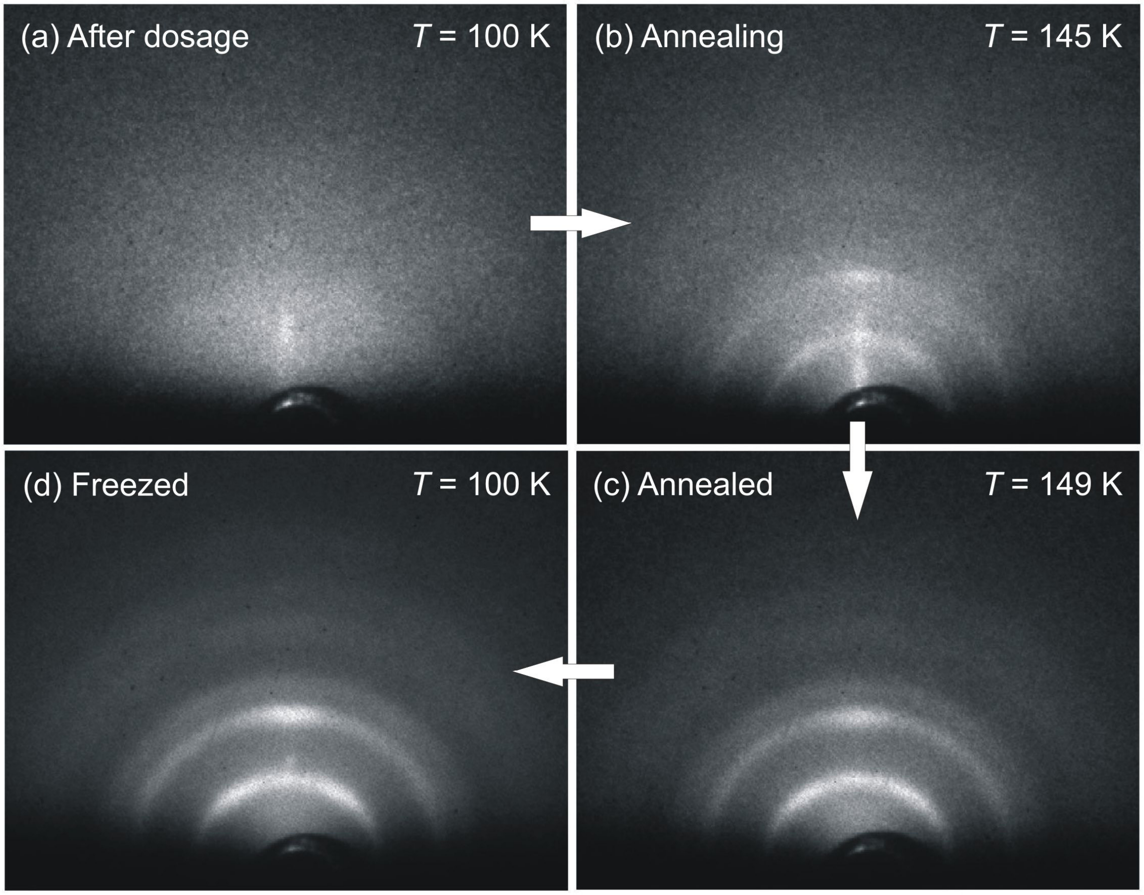

Fig. 1. Diffraction patterns of vapor-deposited water on H/Si(111) at various conditions. (a) Diffraction pattern after the deposition of water molecules at a surface temperature of $T = 100$ K. The diffuse scattering without distinct diffraction features indicates that the water assembly is in an amorphous state. The faint rod-like feature in the center is from the underlying silicon substrate. (b) Diffraction pattern at $T = 145$ K during the process of thermal annealing. Features of Debye–Scherrer diffraction rings appear, indicating the formation of randomly oriented crystallites in the assembly. The rod-like feature in the center is again from silicon. (c) Diffraction pattern at $T = 149$ K after full crystallization of the water assembly into polycrystalline ice. The better diffraction of ice crystallites fully obscures that of the substrate. (d) The pattern of the thermally annealed ice assembly maintained at $T = 100$ K.

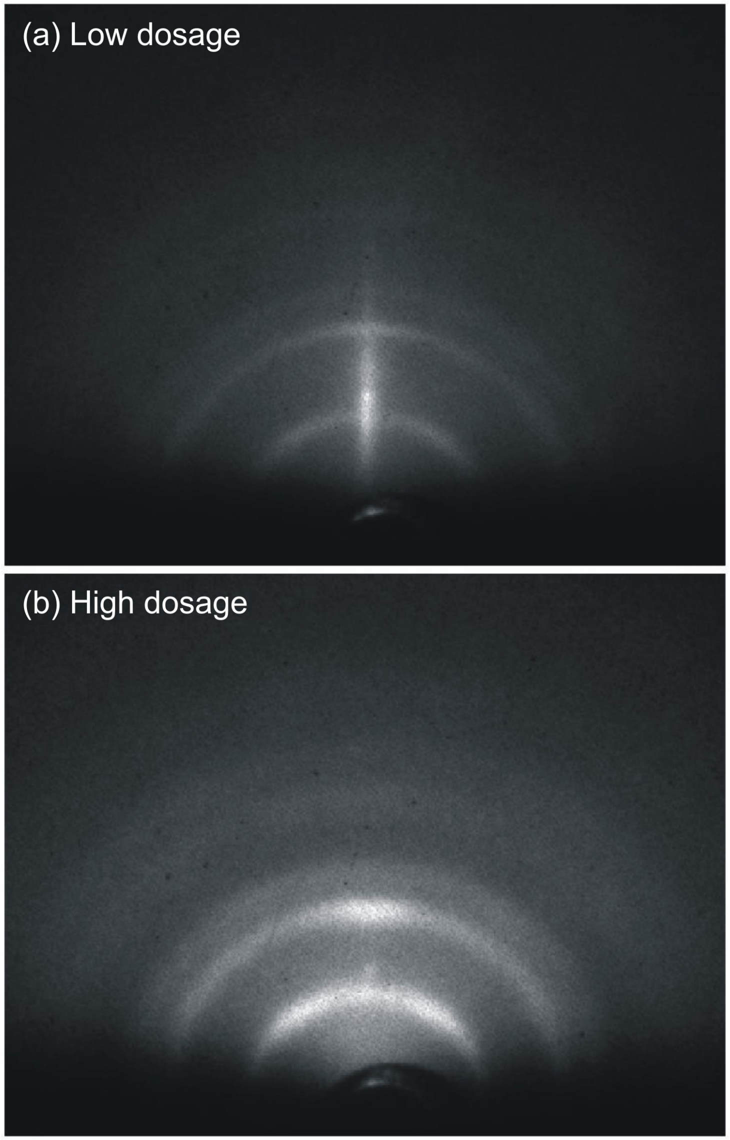

Fig. 2. Diffraction of ice assemblies with different film thickness. (a) The pattern from a thin interfacial ice layer (lower water dosage with a dose time of 10 minutes). The ring intensities are relatively weak, and the thickness of the ice assembly is not enough to block the electron probing of the silicon substrate, which gives the rod-like diffraction feature at a small incidence angle. (b) The pattern from a thick ice layer (higher water dosage with a dose time of 45 minutes). The film thickness is now larger than the penetration depth of 30-keV electrons at this incidence angle, and therefore diffraction of silicon is almost obscured. The increasing prominence of arcs on the first two rings arises from the crystallites with {110} preferred orientation, suggesting their locations above the polycrystalline component (see Text and Figs. 4 and 5).

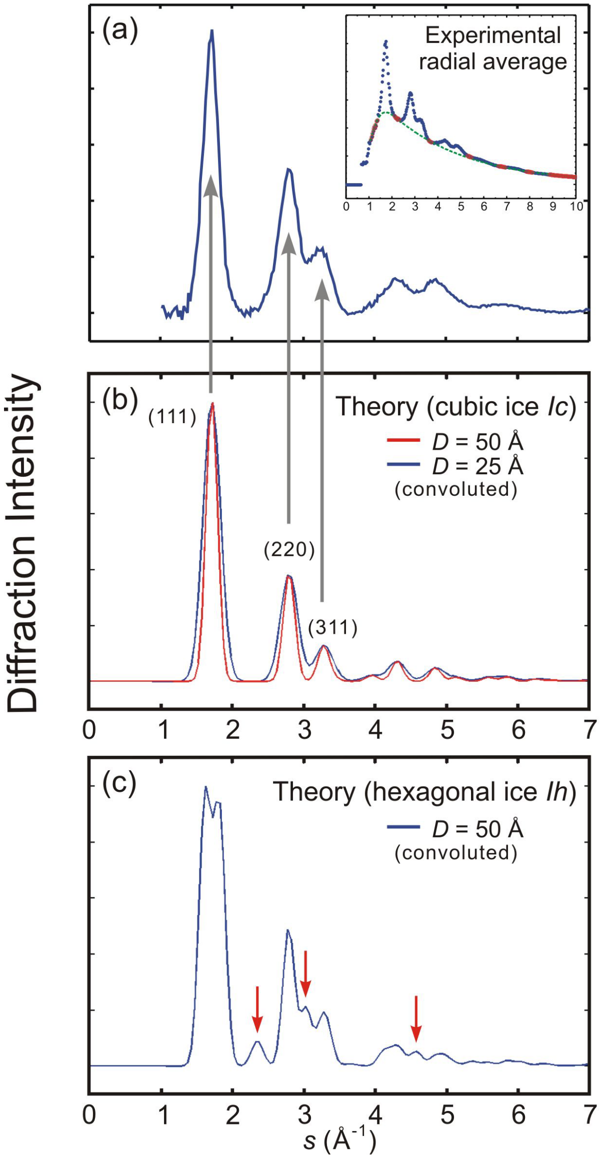

Fig. 3. Radially averaged diffraction profile and calculated patterns for two polycrystalline polymorphs of ice. (a) Shown in the inset is the original radial average of the diffraction pattern obtained (blue dots), which contains a diffuse background that was fitted considering the regions with no peaks (red dots) and subsequently removed (green dashed line). The final result emphasizes the Bragg diffractions arising from the ordered structure of ice. (b) Calculated polycrystalline diffraction patterns for the cubic-ice polymorph, ice *Ic*, with average crystallite sizes of 25 Å (blue) and 50 Å (red); the width contains convolution of the instrumental electron spread. The three most intense diffractions are labeled with the corresponding Miller indices. (c) Calculated polycrystalline diffraction pattern for the hexagonal-ice polymorph, ice *Ih* ($a = 4.506$ Å, $c = 7.346$ Å), with an average crystallite size of 50 Å. Red arrows indicate the diffraction peaks that are missing in the observed pattern illustrated in panel a.

experimental repetition rate of 1 kHz.

Structure of Interfacial Water

A. Diffraction and Structural Determination

After vapor deposition of water onto H/Si(111) at $T \sim 100$ K, the diffraction pattern from the silicon substrate is replaced by diffuse scattering, indicating the absence of structural order in the initially formed amorphous phase of water (Fig. 1a). As T increases at a ramp rate of ~7.5 K/min, new features in the diffraction pattern vaguely appear at $T > 135$ K; at around 145 K, the formation of Debye–Scherrer diffraction rings is observed (Fig. 1b), which become more distinct at $T = 149$ K (Fig. 1c). After lowering the substrate temperature back to 100 K the ring pattern remains prominent (Fig. 1d). Such a pattern change after the annealing process is a clear indication of a phase transition in the interfacial water layers from an amorphous structure, with only short-range order, to a crystalline phase of ice exhibiting longer-range ordering of water molecules. This transformation at low temperature has also been observed previously (*29-31*). It is noted that the ice film thickness, depending on dose time, is on the order of 10 nm estimated from the electron penetration depth at 30 keV (see Fig. 2).

The appearance of Debye–Scherrer rings is characteristic of diffraction from a polycrystalline sample comprising a large number of randomly oriented small crystallites (*32*). Here, the diffraction intensity distribution depends solely on the magnitude of the momentum transfer coordinate s, and therefore we may represent this distribution as a function of s by radially averaging the pattern. A typical intensity curve is plotted in the inset of Fig. 3a, featuring several diffraction peaks superimposed on a decaying diffuse background. This background contains contributions from inelastic scattering and thermal diffuse scattering (*33*), as well as any remaining amorphous water (*29, 34*); toward low s values, it also exhibits a sharp decrease that corresponds to the shadow of the sample in the direction of the electron beam propagation (i.e., the shadow edge; see also Fig. 1). In order to subtract the background and hence focus on the diffraction peaks, we select the regions with no Debye–Scherrer ring feature and fit them with the function of an exponential rise (for the shadow edge) times an exponential decay (for the gradual decreasing part) (*35*). The final pattern that emphasizes the elastic scattering contribution from Bragg diffractions of the interfacial ice is shown in Fig. 3a.

It is known that two ice polymorphs are possible at our experimental conditions: ice of the cubic form *Ic* (space group $\mathrm{Fd}\overline{3}\mathrm{m}$) (*36*) and that of the common hexagonal form *Ih* (space group $\mathrm{P6_3/mmc}$) (*37, 38*). In Fig. 3, panels b and c, we present the radially averaged diffraction intensity curves calculated for the two polycrystalline polymorphs *Ic* and *Ih*, respectively (*39*). It is evident that the peak positions in our diffraction data are in excellent agreement with those of ice *Ic*, thus confirm the assignment of ice *Ic* to the structure of interfacial ice crystallites formed on H/Si(111) in vacuum; the possibility of formation of ice *Ih* can be confidently excluded by the absence of the characteristic ice *Ih* Bragg reflections at $s = 2.3$, 3.0 and 4.6 Å^{-1} (Fig. 3c). No clear evidence is seen for the formation of hexagonal-like stacking faults, as was observed in other studies of ice *Ic* crystallization (*31, 36*), although we acknowledge that the (111) diffraction peak width may obscure such features.

In a previous study of interfacial water by this laboratory on a *hydrophilic* surface, chlorine-terminated Si(111), the appearance of distinct diffraction spots superimposed upon diffraction rings indicated the formation of an ordered, crystalline ice *Ic* structure as well as a randomly oriented polycrystalline component (*24*). In the present study on a *hydrophobic* substrate, however, no Bragg spots but Debye–Scherrer diffraction rings are observed, signifying that the ice *Ic* crystallites do not adopt a well-defined orientation with respect to the silicon substrate. The lack of orientational order among the ice crystallites originates from two reasons: (i) from the energetics point of view, stronger intermolecular hydrogen bonds and weak water–substrate interfacial interaction make longer-range ordering of crystalline ice unfavorable, and (ii) the atomically flat H/Si(111) surface provides no template structure for guided growth of ice along a certain direction (Ch. 9). As a result of no guiding force, clusters of water molecules form small ice crystallites during the annealing process without extensive crystalline growth.

Given the diffraction peak width of ~0.25 $Å^{-1}$ and the instrumental electron spread of ~0.16 $Å^{-1}$, the diameter of ice crystallites is estimated to be ~30 Å by both diffraction simulation (Fig. 3b) and Scherrer formula (Eq. 23 of Ch. 2). However, this diameter can be as large as 50 Å or more if the amorphous component in the ice assembly (*29*), which effectively increases our diffraction peak widths and consequently leads to an underestimated crystallite diameter, is taken into account. The difference in crystallite size among previous studies and our result is noted (*29, 30, 34, 36, 40, 41*), which stems most likely from the different crystallization conditions employed and also provides a reasonable explanation for the stacking fault features often observed in larger crystallites of ice *Ic* (*34, 36, 42*).

B. Ice Crystallites with Preferred Orientation

A closer look into the intensity distribution along the first two diffraction rings shows that some regions are relatively more intense (Fig. 2b). The broad arcs of additional intensity superimposed upon the circular rings are indicative of certain preferred crystallite orientation, or texture, within the polycrystalline sample (*32*),

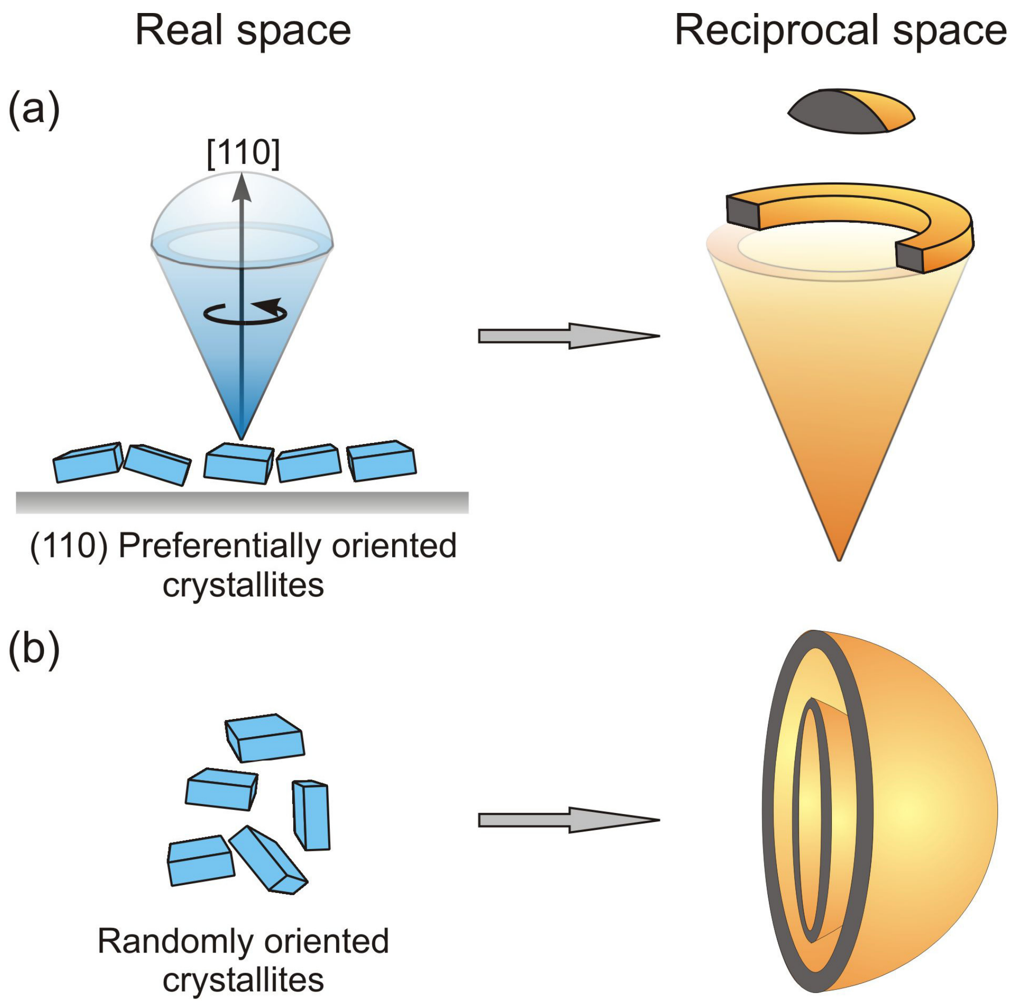

Fig. 4. Illustration of the correlation between crystallite orientation in real space and diffraction in reciprocal space. (a) For crystallites with (110) preferred orientation, their [110] vectors lie roughly perpendicular to the substrate surface with angular deviations that are contained in a spherical cone (left). The angular span of this cone is reflected in reciprocal space, showing a cylindrical symmetry in the resulting intensity distribution (right). The dark gray regions indicate the intersections with the Ewald sphere that give rise to the broad arc features in the diffraction pattern. (b) All orientations are populated for randomly oriented crystallites, assuming that a sufficient number of crystallites are probed (left). The corresponding reciprocal space contains a set of concentric spherical shells (right), giving rise to the Debye–Scherrer rings in diffraction (dark gray regions).

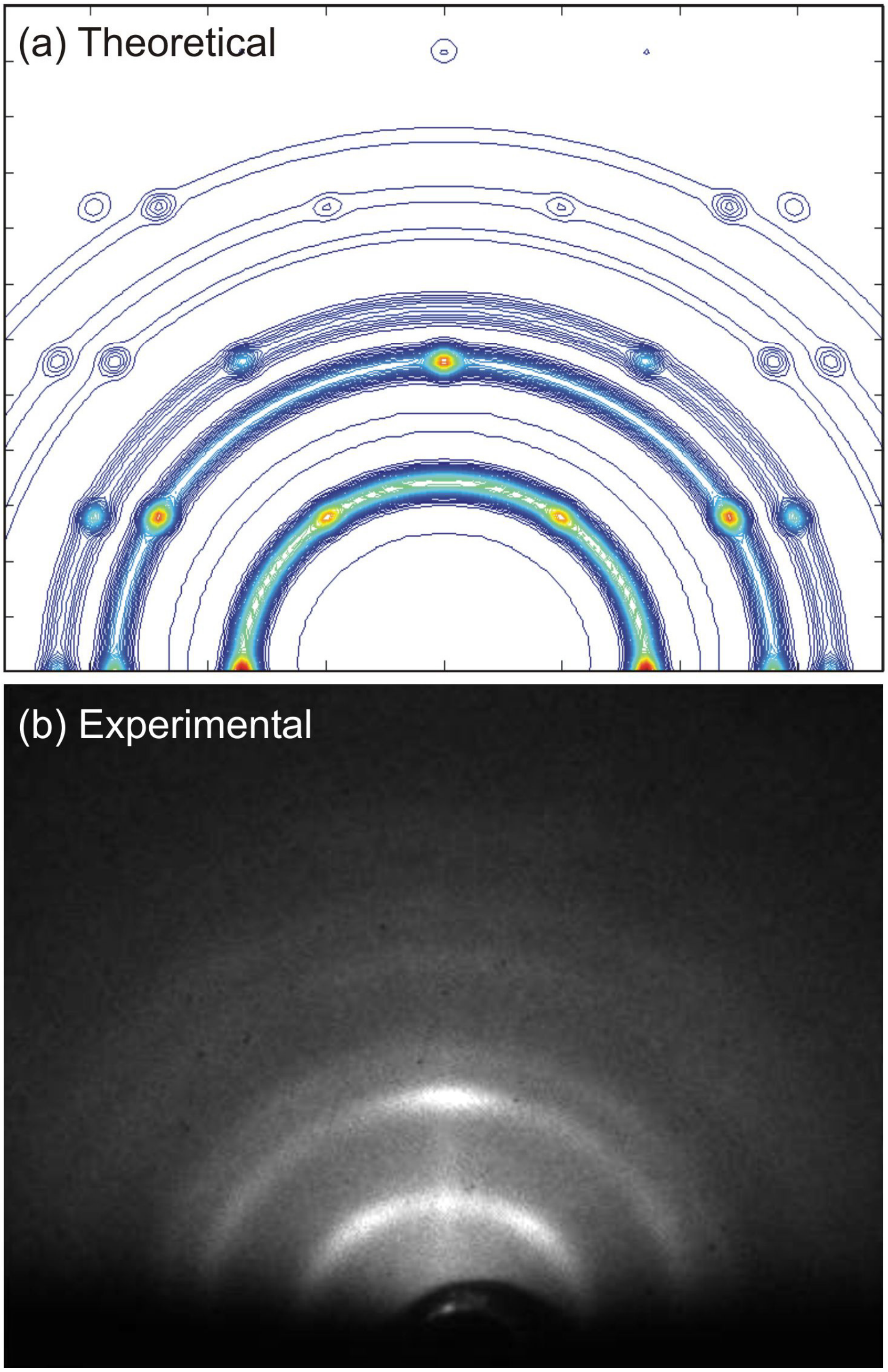

Fig. 5. Comparison of (a) theoretical simulation and (b) experimental observation of diffraction from an interfacial ice assembly containing both randomly and preferentially oriented crystallites of ice *Ic*.

namely, a significant number of ice *Ic* crystallites more or less oriented with a specific lattice plane parallel to the substrate surface but with random rotation around an azimuthal axis approximately perpendicular to the substrate. Figure 4 illustrates the correlation between the real-space morphology and the reciprocal-space intersection with the Ewald sphere (diffraction pattern), showing that crystallites with preferred orientation remove the spherical symmetry of the reciprocal space for a randomly oriented polycrystalline sample and result in localized intensity distribution.

From the observation of an apparent intensity increase in the middle region of the (220) ring (Fig. 2b) and simple geometrical argument, it is straightforward to conclude that the preferred orientation is the {110} planes [(110) and five other equivalent sets of planes in the cubic structure] being approximately parallel to the substrate surface. This assignment is further supported by the appearance of two arcs of increased intensity on the (111) ring: the angle between the vectors from the direct beam origin to the center of an arc on the (111) ring and to the middle of the (220) ring is approximately 35°, coinciding with the angles between the (111) $[(11\bar{1})]$ and (110) planes in the cubic structure. In Fig. 5a, the simulated pattern for coexisting randomly and preferentially oriented crystallites of ice *Ic* is presented, and the various regions that show an intensity increase match reasonably with the experimental data (Fig. 5b). The fairly extended arc (with a span of ~30°) observed in the middle of the (220) ring indicate that the angular distribution of the preferred [110] axis is within a ~15° cone around the substrate surface normal (Fig. 4a).

Furthermore, it is found that the {110} preferred orientation is more favored by those crystallites near the ice–vacuum interface. It is noted from the experiments that the diffraction feature of intensified arcs is particularly pronounced from a thick ice assembly

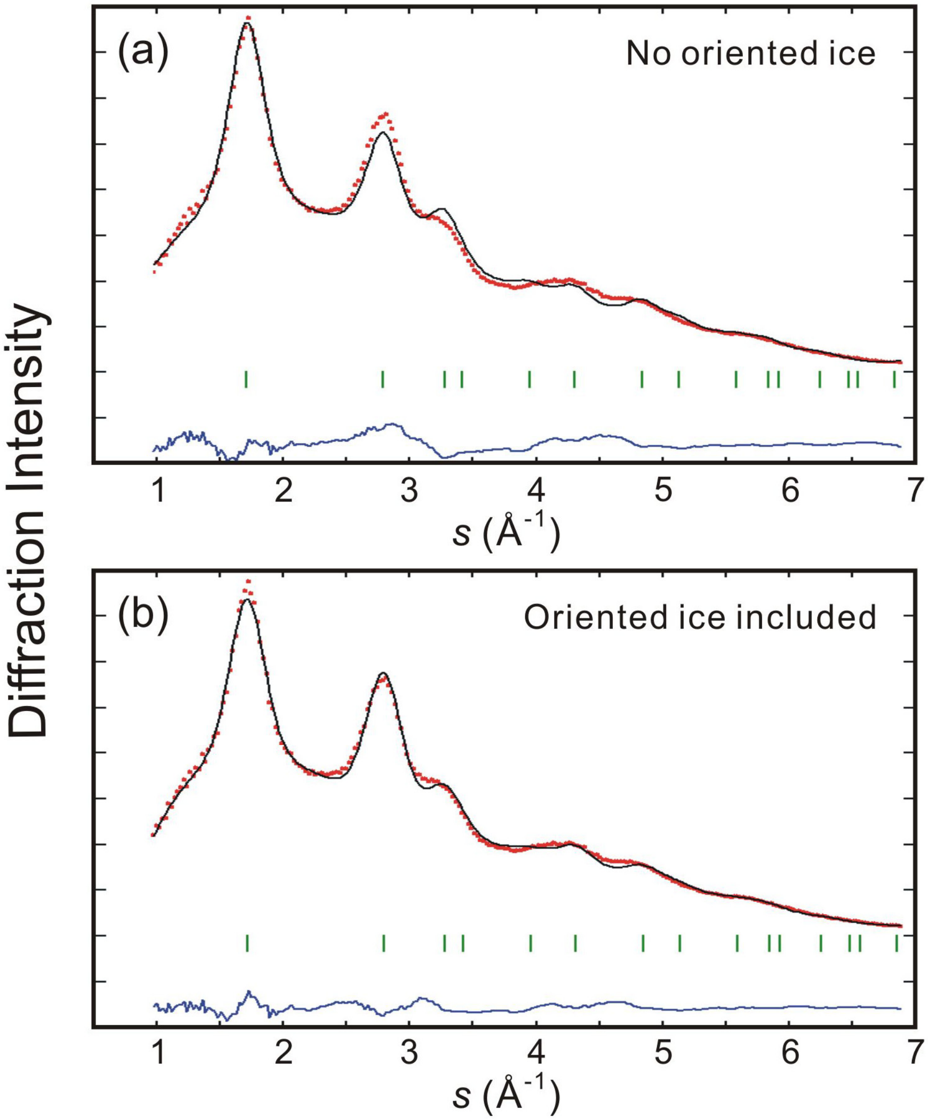

Fig. 6. Comparison of simulated diffraction curve (black line) and radially averaged diffraction profile obtained experimentally (red dots). (a) For an assembly containing only crystallites of random orientation; the refined factor for overall isotropic atomic displacement was $B = 1.24$ Å^2. (b) The Rietveld preferred orientation function is included in the simulation of diffraction pattern. The refined factor for overall isotropic atomic displacement was $B = 1.55$ Å^2, which matches well with the reported value for oxygen (*36*). The blue curve in each panel is the residual difference between the simulation and experiment.

(Fig. 2b), compared with that from a thinner one (Fig. 2a). Such an observation signifies the probing, and hence the presence, of the preferred oriented crystallites from above; they are not located only next to the hydrophobic surface because, with the randomly oriented component covering above, more homogeneous intensity along the diffraction rings would be expected for a thicker ice assembly, given the finite penetration depth of electrons. From the viewpoint of energetics, among all low-indexed crystal planes, the {110} preferred oriented ice is able to have many in-plane hydrogen bonds and leave the fewest dangling O–H bonds pointing directly into vacuum, thus it becomes a more stable structure near the ice–vacuum interface.

The extent of preferred orientation and refined lattice constant are obtained by least-squares analysis, or Rietveld refinement (*43*), of the radially averaged diffraction pattern (*44, 45*). Here, for the consideration of purely random orientation of crystallites, the relative Bragg peak intensities were fixed, being calculated from the known structure of ice *Ic*. However, parameters defining the background, Bragg peak positions and shapes were simultaneously refined to optimize an agreement between the experimental and simulated radial curves (*46*). The result is shown in Fig. 6a, with the weighted-profile R-value being $R_{\mathrm{wp}} = 3.6$ % (the Bragg R-value being $R_{\mathrm{Bragg}} = 8.2$ %) (*47*); the difference curve indicates rather clear discrepancies between the two patterns, particularly in the intensities of the first two Bragg peaks.

With preferred oriented ice included in the analysis, the experimentally observed pattern can be better modeled using the method of Rietveld (*43*). The Bragg peak intensities $I(hkl)$ are subsequently multiplied by the factor $\kappa + (1-\kappa)\cdot\exp(r\alpha^2)$, where κ is the fraction of polycrystalline component in the sample, r an optimizable quantity related to the diffraction strength of preferred oriented ice, and α the acute angle between the

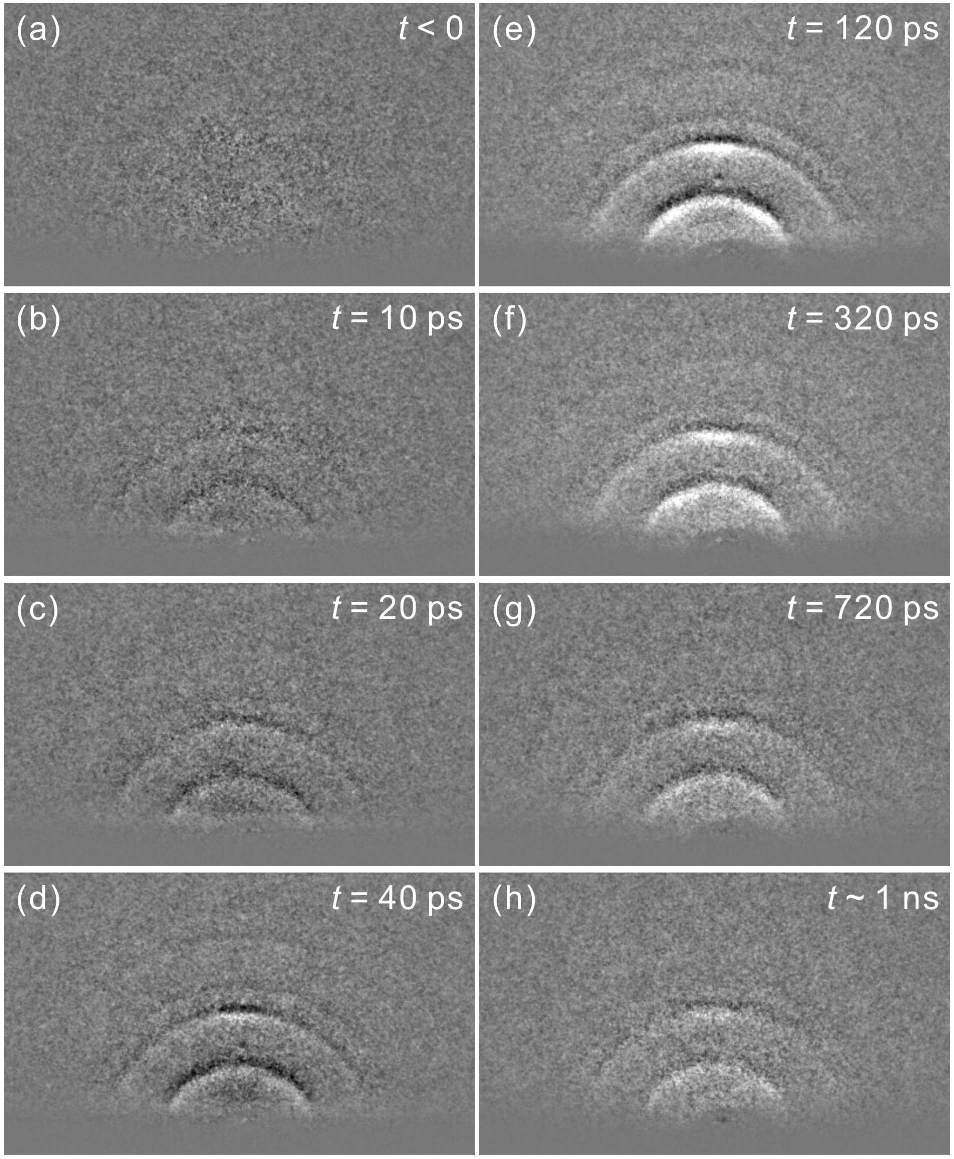

Fig. 7. Diffraction difference images at various delay times. The reference time frame is at $t = -380$ ps. (a) No diffraction difference is detected at negative times. (b–c) Depletion of the intensities of Debye–Scherrer rings is noticed after the substrate T-jump induced by a femtosecond infrared pulse. (d–e) Enhancement of the ring intensities underneath the depletion indicates shifts of the original ring positions toward smaller s values. At $t \sim 100$ ps the diffraction difference reaches its maximum. (f–h) Decay of the diffraction difference means the recovery of diffraction patterns toward the original one, which signifies that the polycrystalline ice assembly is restructuring to the original ground state.

plane (*hkl*) and the plane of preferred orientation. The effect of this procedure is to increase the simulated intensities of those Bragg reflections arising from planes more parallel to the preferred orientation [the (110) plane in the present case] and decrease those arising from planes at a large angle to the plane of preferred orientation. The result in given in Fig. 6b, showing a clear improvement in the level of agreement between the calculated and experimental patterns, with R_{wp} decreasing to 2.1 % (R_{Bragg} to 2.7 %). The refined value of $\kappa = 0.44$ signifies that a slightly greater fraction (56 %) of the ice assembly probed by electrons is roughly {110}-oriented. The value of $r = -2.53$ is consistent with the presence of plate-like crystallites lying parallel to the surface. Lastly, the unit cell parameter determined after least-squares fitting agrees well with the value reported previously [a = 6.35(3) Å versus a = 6.358 Å (*36, 40*)].

Dynamics of Interfacial Water: Results and Analysis

The dynamics of interfacial ice on H/Si(111) was monitored as a function of time following the substrate *T*-jump induced by the infrared laser pulse. The diffraction difference images, obtained by subtracting a reference frame at negative time from patterns at selective delay times, are shown in Fig. 7. The zero of time was consistently determined in two independent experiments to be the onset of intensity change of the specular spot from the silicon substrate. The fact that no diffraction difference was observed at negative times (Fig. 7a), as expected, signifies full recovery of the ice assembly in less than one millisecond given by the repetition rate (1 kHz) of our system. Also, from scan to scan the diffraction images did not exhibit substantial changes, indicating the lack of a major sublimation loss of interfacial water on the time scale of our experiment. Therefore, the long-term stability over many pulses and scans was

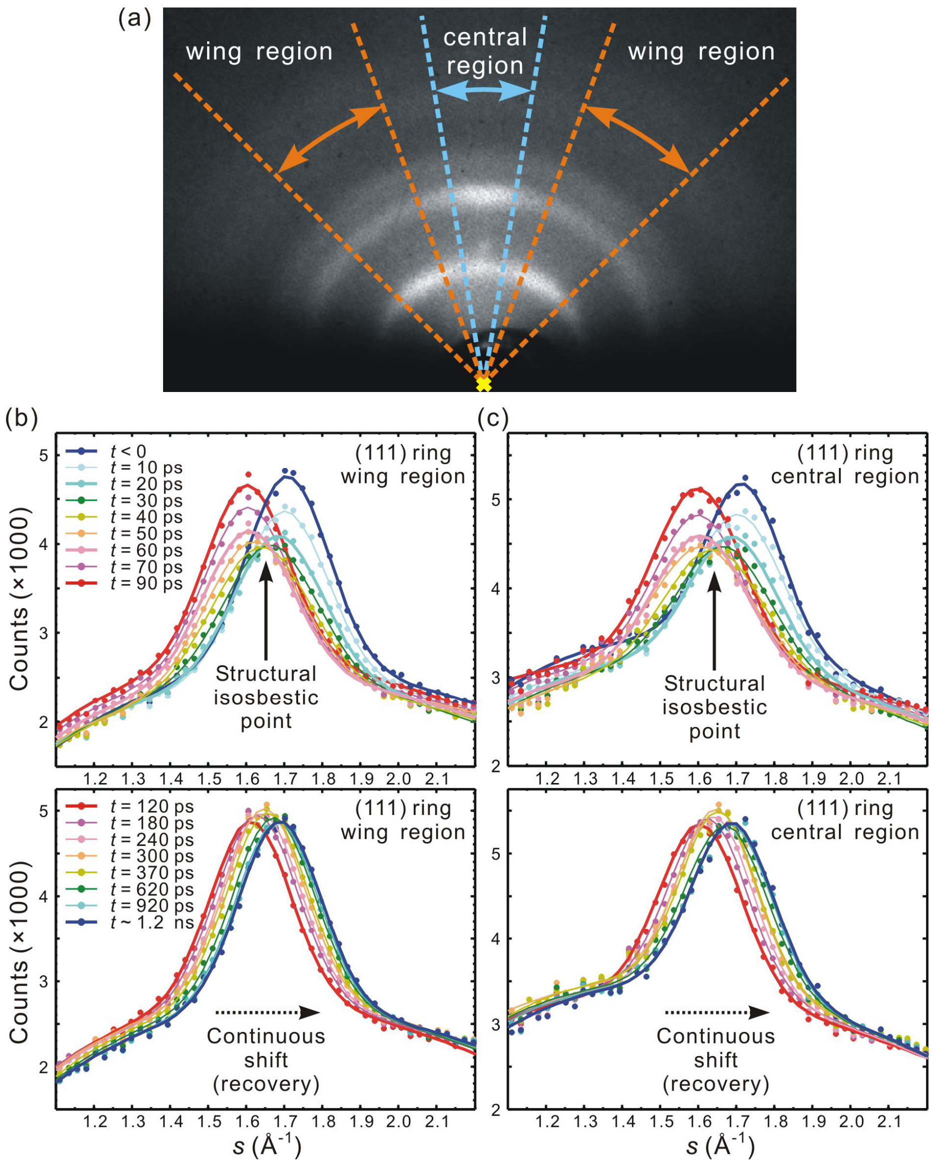

Fig. 8. Analysis of diffraction at different delay times and for different regions. (a) Diffraction pattern with indication of two types of regions considered for radial averaging (with respect to the central axis, ±20° to ±45° for the red regions and –10° to 10° for the blue). The yellow cross marks the origin of Debye–Scherrer rings. (b) The family of curves for the (111) diffraction ring at early times (upper) and longer times (lower), which are obtained by radially averaging the wing regions without any background removal. (c) The family of curves from the central region for early times (upper) and longer times (lower). The same behavior shown in panels b and c indicates the negligible role of crystallite orientation in the dynamics of ice (see Text for the four stages of diffraction change observed). The initial peak fluence for silicon *T*-jump is 77 mJ/cm^2.

maintained even in this volatile system.

Immediately after the heating pulse impinges on the substrate (i.e., the time zero), depletion of the diffraction ring intensities was observed (Fig. 7, panels b and c), indicating that partial depletion of the original structure, whether by larger atomic motions or through ultrafast melting, takes place at this stage. Later, as presented in Fig. 7, panels d and e, the difference patterns show shifts of the original rings toward slightly smaller s values; the diffraction difference is most distinct at $t \sim 100$ ps. Such diffraction ring shifts are clear indication of an expanded structure in ice on this time scale. After the maximum change is reached, the ice assembly restructures, recovering toward the initial structure, as evidenced by less and less diffraction difference at longer times (Fig. 7, panels f to h). After $t = 1$ ns, only a residual amount of change remains (Fig. 7h), which means that the full recovery of the system is likely on the nanosecond time scale.

In order to investigate the dynamics quantitatively, radial averages of the diffraction pattern at each delay time were performed over two different angular ranges (Fig. 8a), to first examine any difference in the structural dynamics between randomly oriented and preferentially oriented ice *Ic* crystallites (*48*). From the comparison between Fig. 8, panels b and c for the (111) ring at an excitation fluence of $F_{max} = 77$ mJ/cm^2 at the peak, it is shown that all ice *Ic* crystallites, with or without the preferred orientation, exhibit the same type of structural evolution with no phenomenological difference in behavior (thus the crystallite orientation effect can be neglected in the following analysis and discussion): (i) for the first 20 ps (Stage I), a decrease in diffraction intensity without a significant profile movement, (ii) from $t = 20$ ps to $t = 60$ ps (Stage II) the observation of a clear profile shift, with all curves crossing at the same point (a “structural isosbestic” point), (iii) from $t = 60$ ps to $t = 120$ ps (Stage III), an increase in diffraction intensity at

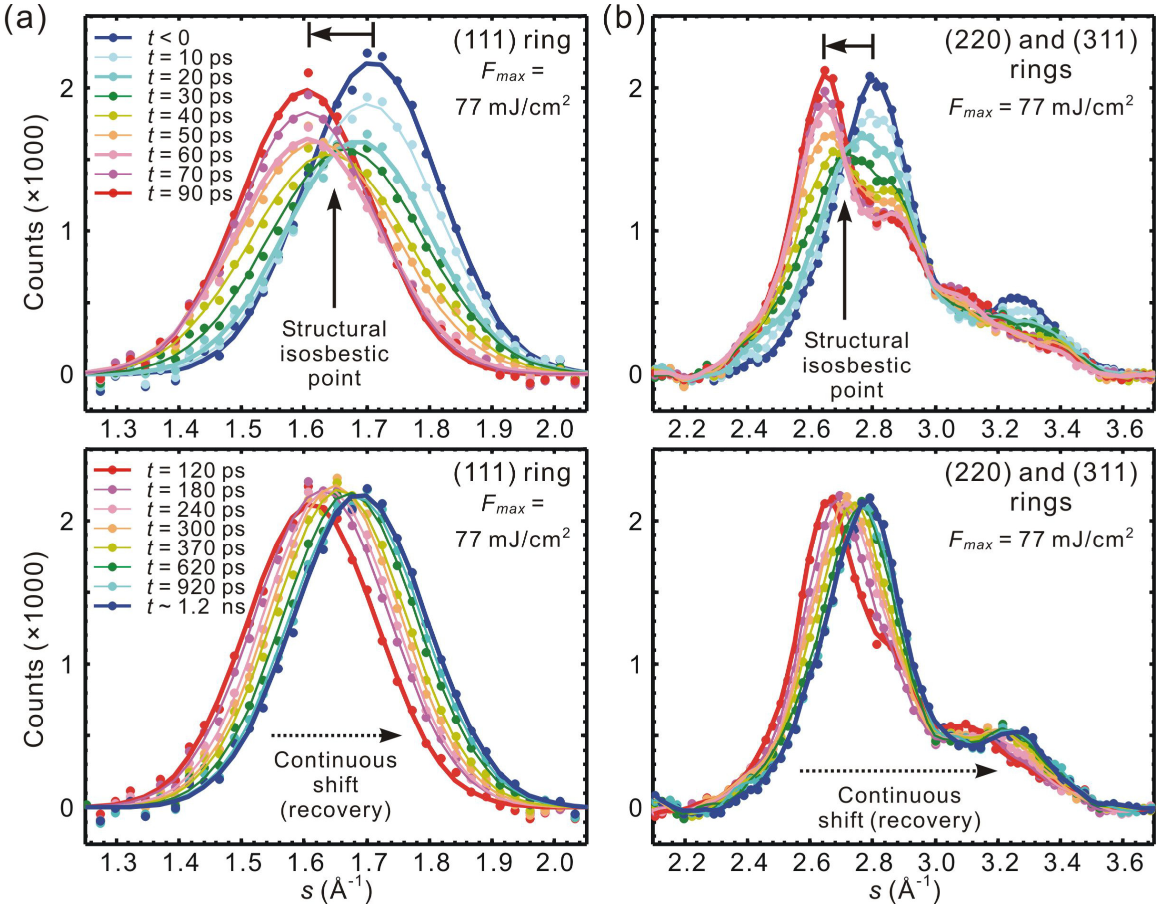

Fig. 9. Diffraction profiles at different times after removal of the diffuse background. Shown are the family of curves for (a) the (111) ring from the wing regions and (b) the (220) and (311) rings from the central region, as indicated in Fig. 8a. At early times, diffraction profiles go through stages of intensity decrease, curve crossing at the same point termed a structural isosbestic point, and intensity recovery (upper panels). At longer times, diffraction profiles move toward their original positions continuously, with their intensities maintained at the same level (lower panels). The initial peak fluence for silicon *T*-jump is 77 mJ/cm^2.

the new peak position, and (iv) at longer times (Stage IV) the continuous shift of the diffraction profile, not through the isosbestic point, toward the original, equilibrium position (see the upper panels in Fig. 8, panels b and c for the first three stages, and the lower panels for the last stage). It should be noted that the distinct difference in the evolution of the diffraction curves at early and later times is easy to discern, even without removal of the diffuse background. Similar discoveries in interfacial ice on another hydrophobic substrate were also observed (Ch. 9). I shall discuss in detail about the observation of a structural isosbestic point in diffraction and its implication of a nonequilibrium phase transformation at transient times in the next section.

Figure 9 shows the curves for the first three diffraction rings at early and later times for $F_{max} = 77$ mJ/cm^2, after removal of the background. (Except for the studies of fluence dependence, the following results and analysis are from the experiment of a thicker assembly at the excitation fluence of $F_{max} = 77$ mJ/cm^2 at the peak.) The structural isosbestic points manifested from $t = 20$ ps to $t = 60$ ps from the (111) and (220) rings and continuous recovery of their peak positions at later times cause immediate attention. In addition, the aforementioned stages of diffraction change for the evolution of the (111) ring are also valid for that of the (220) ring. Such consistency further confirms that our observations result from the structural dynamics of ice *Ic* crystallites. Also, the phenomena reported here are robust for both thinner and thicker interfacial ice films, as observed in repeated experiments.

Furthermore, the extents of the profile shifts reveal that the structural expansion in ice *Ic* crystallites in the present study is isotropic. An isotropic lattice expansion of the cubic structure requires the position change of the (hkl) diffraction ring, $\Delta s(hkl) = s_0(hkl) - s(hkl)$, to be scaled with $\sqrt{h^2 + k^2 + l^2}$, because the initial interplanar distance

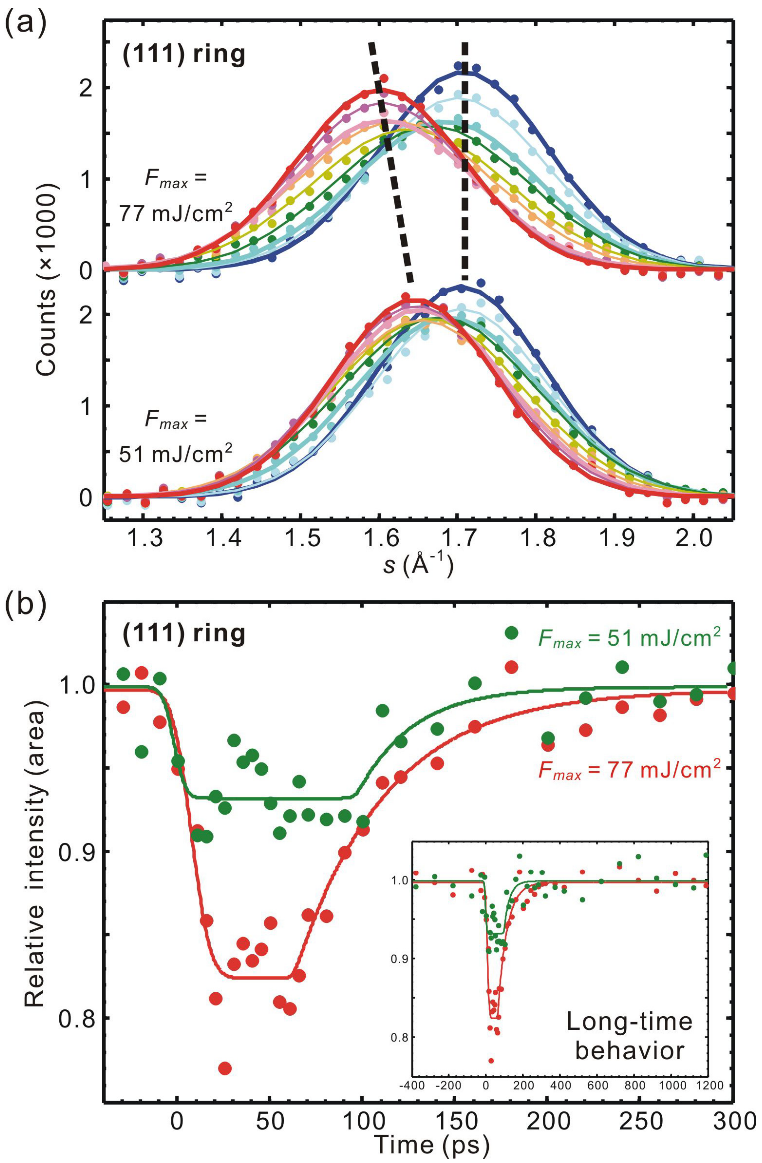

Fig. 10. Early-time evolution of the (111) diffraction at two fluences. (a) Fluence dependence of the curve crossing behavior at a structural isosbestic point. The two dashed lines indicate the original and transformed profile positions. (b) Total intensity under the (111) profile as a function of time. The initial decrease depends on the fluence used, but a common observation is the intensity being at a constant value within a short duration, followed by recovery to the original level and its maintenance at long times (see inset for the long-time behavior).

$d_0(hkl)$ between the (hkl) planes and the lattice constant a_0 satisfy the following relationship, $d_0(hkl) = a_0 / \sqrt{h^2 + k^2 + l^2}$ (the subscript denotes the original value), and the diffraction criterion asks that $s_0(hkl) \cdot d_0(hkl) = s(hkl) \cdot d(hkl) = 2\pi$. That is,

$$\frac{\Delta s(hkl)}{s_0(hkl)} = \frac{d(hkl) - d_0(hkl)}{d(hkl)} = \frac{a - a_0}{a} \tag{1}$$

for a cubic isotropic expansion from a_0 to a. In Fig. 9, upper panels, the (111) and (220) rings are initially located at $s_0(111) = 1.71$ Å^{-1} and $s_0(220) = 2.80$ Å^{-1}, and subsequently transform to the apparent positions of $s(111) = 1.61$ Å^{-1} and $s(220) = 2.64$ Å^{-1}, respectively, at $t = 60$ ps. The fact that the diffraction patterns show the satisfaction of Eq. 1 thus supports our claim.

We also performed the study at different excitation fluences on the substrate surface. As shown in Fig. 10a, the early-time dynamics exhibits the isosbestic point behavior, and the profile shift of the (111) diffraction ring is in proportion to the laser fluence applied. Integration of the intensity under the diffraction profile shows, respectively, an initial total intensity loss, the duration of constant intensity, recovery to the original value and its maintenance for the four stages of change mentioned above, regardless of the different fluences used (Fig. 10b). As discussed in the next section, the intensity depletion signifies the partial destruction or melting at the crystallites' grain boundaries and the later intensity recovery the growth or annealing of crystallites near their boundaries at later times. Moreover, the temporal match of the constant intensity and the isosbestic point behavior gives further evidence for the nonequilibrium phase transformation of ice crystallites induced by the energy transfer from the substrate.

More precise quantification and temporal evolution of the lattice expansion at different fluences require fitting of the diffraction profile. The appearance of a structural

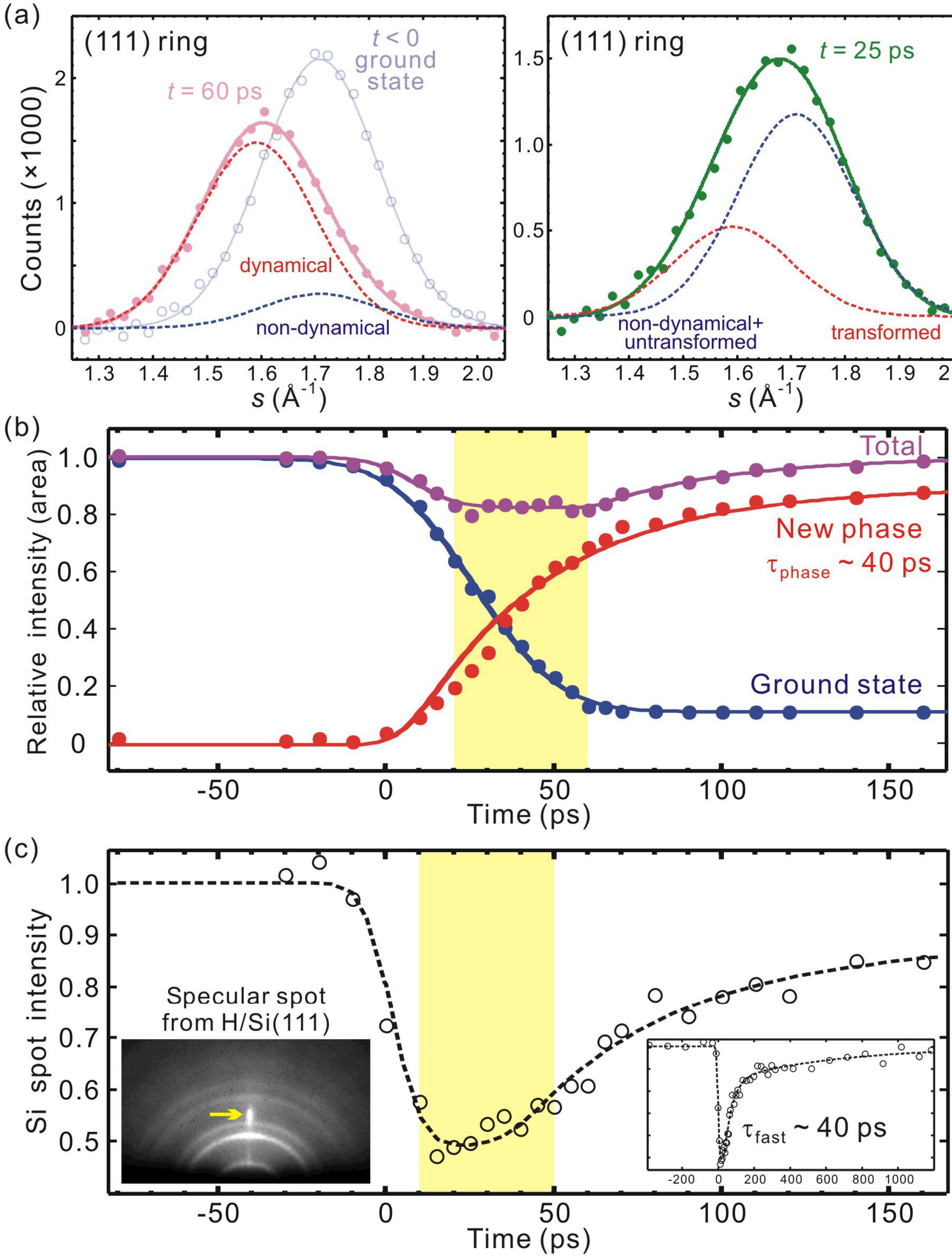

(See next page for the figure caption.)

Fig. 11. Quantitative analysis of the diffractions of interfacial ice and silicon. (a) Fitting of the (111) diffraction profile considering that only two states, the ground state and transformed one, are involved. (Left panel) The light blue circles and pink dots are the data at negative time and at $t = 60$ ps, respectively. A Gaussian profile is fitted to the negative-time data and served as a reference (light blue solid curve). Two Gaussian peaks are used to fit the data at $t = 60$ ps (which is also the end of Stage II), with one being of the same width at the original position but with a variable intensity (blue dashed curve), and the other being of a similar width but having its position and intensity as variables (red dashed curve). The former peak represents the nondynamical portion in the diffraction and the latter the dynamical portion (see Text for details). The final result of the two-Gaussian fit is shown as the pink solid curve. (Right panel) Two-Gaussian fit to the data at $t = 25$ ps (green dots), as an example showing the fitting procedure for all profiles at early times. The blue dashed curve has the same width and position as those of the negative-time profile (light blue solid curve in the right panel) but with a variable intensity, representing the sum of the nondynamical and untransformed portions in the diffraction. The red dashed curve has the same width and position as those of the transformed peak (red dashed curve in the right panel), with its intensity as a variable. The final result is shown as the green solid curve, which nicely accounts for the small asymmetry that appeared in the experimental data at $t = 25$ ps. The agreement between the data and the fit at each delay time has also been checked. (b) Depletion of the ground state of ice structure (blue) and growth of the new phase (red), together with the sum of their proportions (purple). The yellow region indicates the duration of Stage II when the curve crossing behavior at a structural isosbestic point manifests itself. Note that the total intensity also remains constant during this time range. The transformation into the new phase follows approximately a function of exponential rise and has a time constant of $\tau_{\text{phase}} \sim 40$ ps. The slight delayed start in the growth with respect to the depletion of the ground state signifies the structural dynamics of ultrafast melting in the first stage (see Text for details). The small constant level of the ground state after Stage II is due to the nondynamical portion in the diffraction (Fig. 10a, blue dashed curve in the left panel). (c) Intensity evolution of the specular spot from the silicon substrate (pointed by a yellow arrow in the left inset). The yellow region indicates the time range when the specular intensity is at its minimum level. The right inset shows the long-time behavior.

isosbestic point at early times signifies the conversion involving two distinct states, the untransformed ground-state structure and a transformed, expanded one, thus making it legitimate to fit the early-time (111) diffraction profile by two Gaussian peaks at fixed positions, with variable intensities representing the interconverting populations between the two. The ground-state peak is centered at $s_0(111) = 1.71$ Å^{-1} (the negative-time value) and the transformed-state one at a position determined from the two-Gaussian fit using the diffraction profile at $t = 60$ ps, i.e., the end of Stage II (Fig. 11a, left). During Stage I and II, the width for the ground-state peak remains the original value of ~0.25 Å^{-1} determined previously. Also, the transformed-state peak has a width similar to or marginally larger than the ground-state value, because the proper description for the dynamical transformation in this study asks the average size of the expanded ice crystallites to be about that of the original; the width of a diffraction profile is contributed by the size of the electron beam (a constant value), the broadening effect described by the Scherrer formula due to the finite size of ordered structure (presumably a nearly constant effect), and electron refraction due to the shape of the crystallites (a small and nearly constant effect; see Chs. 2 and 5).

Figure 11a shows the results of profile fitting at two different times as examples, and Fig. 11b the relative populations for the ground-state and transformed structures, together with their sum. We find that the peak for the transformed structure is centered at $s = 1.59$ Å^{-1} for $F_{max} = 77$ mJ/cm^2, which corresponds to a 7.6% increase in the lattice constant of ice crystallites, to $a = 6.84$ Å. The existence of a constant, nondynamical portion for all times results from the electron probing of unexcited regions due to the overlap difference between the laser-excited area and the electron beam footprint, thus is subsequently removed from the diffraction profiles in Stage III and IV to eliminate its

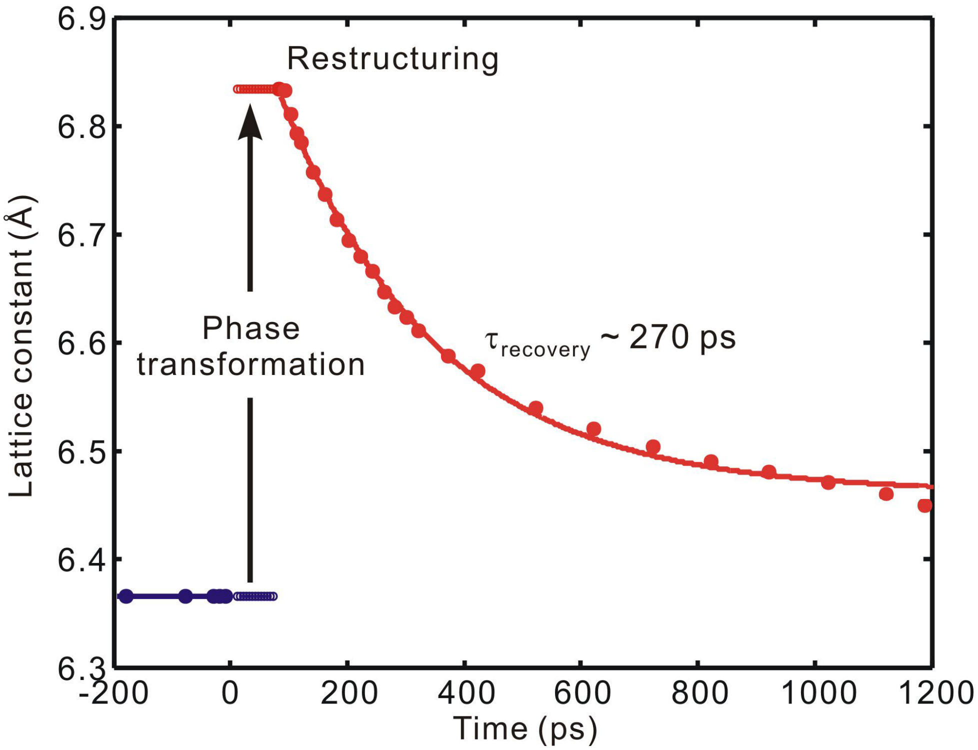

Fig. 12. Restructuring of the expanded lattice at longer times. The continuous recovery of the lattice constant (red dots) to the equilibrium value (blue dots) exhibits an apparent form of single exponential decay, with a time constant of $\tau_{\text{recovery}} \sim 270$ ps. The remaining 20% change at $t = 1.2$ ns takes longer time to diminish.

interference with the recovery of the transformed phase (see the constant residual level of the blue curve after $t = 60$ ps in Fig. 11b). The original structure is found to disappear with a time constant of $\tau_{\text{melting}} \sim 20$ ps, and the new phase grows with a time constant of $\tau_{\text{phase}} \sim 40$ ps. The sum of the two phases reproduces the total intensity evolution show in Fig. 10b. For comparison and later discussion about the energy transfer across the interface that induces the dynamics in ice, intensity of the specular spot from the substrate (seen in an experiment with coverage of interfacial ice, at a larger electron incidence angle) is plotted as a function of time in Fig. 11c.

After the mature structural transformation is reached, the transformed ice

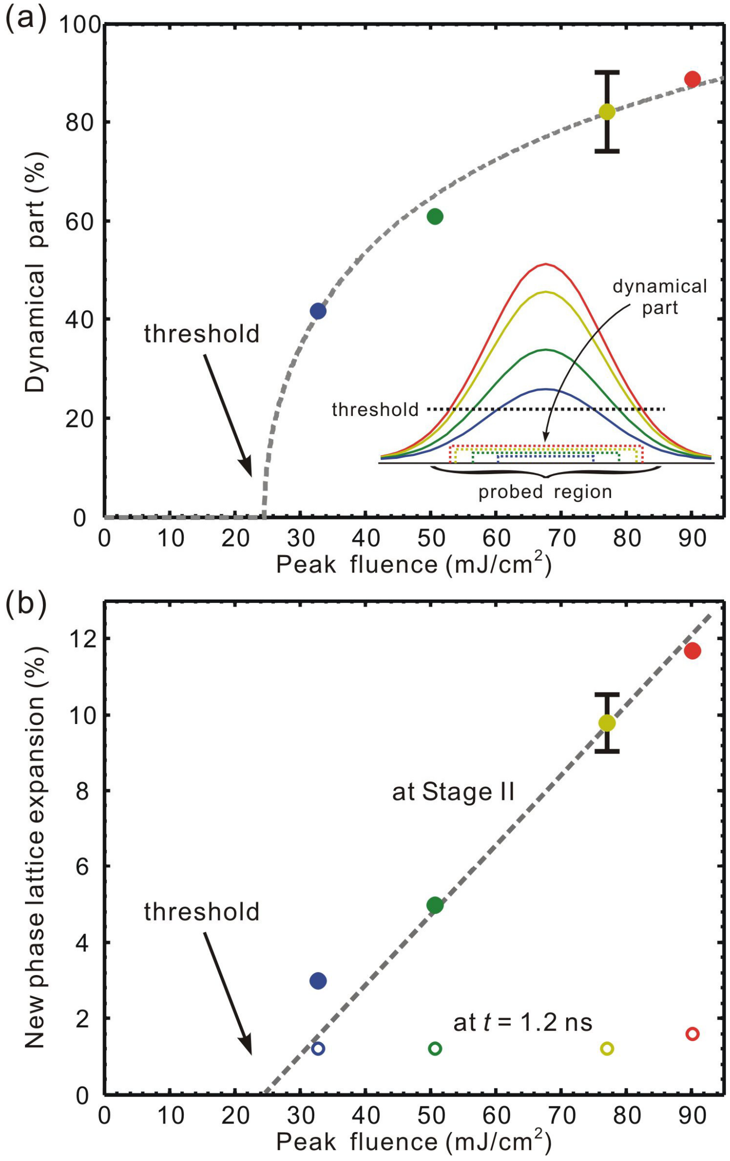

Fig. 13. Fluence dependence of (a) the dynamical portion in the diffraction of ice and (b) the corresponding lattice expansion of the new phase (solid dots); the error bar is also given for each panel. The nonlinearity is noted from the missing of the origin in the trend. By considering an effective threshold for significant two-photon absorption that is able to initiate dynamics of the interfacial ice above (panel a, inset), we can fit the fluence dependence of the dynamical portion with the gray dashed line, where the threshold value is about 25 mJ/cm^2 (see Text for details). A similar threshold is also found in (b). At t = 1.2 ns, the remaining lattice expansion of the transformed part is nearly fluence independent (open circles).

structure behaves collectively and starts its recovery as a unit. Therefore, the diffraction curves in Stage III and IV (after removal of the nondynamical portion mentioned above) can be fitted by a single Gaussian profile. From the observed peak shifts at different times we obtained the lattice constants as given in Fig. 12. The expanded ice *Ic* crystallites are seen to restructure continually to the ground-state structure, with an apparent time constant of $\tau_{\text{recovery}} \sim 270$ ps. This time constant is found to exhibit a slight dependence on the thickness of the ice assembly, varying from the given number for a thicker film to ~200 ps for a thinner one. The restructuring of ice is close to 80% complete in 1.2 ns, and the remaining lattice expansion (~1.5% of the lattice constant) is likely to diminish on the nanosecond scale.

More complete fluence-dependent studies were carried out on another ice assembly to investigate the extent of lattice expansion in the transformed phase. Interestingly, from fitting of the diffraction profile at $t = 60$ ps, it is found that the nondynamical portion varies with the excitation fluence on the substrate, in a nonlinear fashion (Fig. 13a); particularly, for a fluence below 30 mJ/cm^2 at the peak, the nondynamical portion reaches 100% because nearly no diffraction shift was measured. Consistently, a threshold behavior seems to also appear in the fluence dependence of the obtained lattice expansion (Fig. 13b, solid dots). At the highest fluence used, however, the isotropic structural expansion reaches ~12% of the lattice constant, whose atomic movements seem to exceed the equilibrium Lindemann limit for thermal melting, i.e., when the root-mean-square amplitude of thermal vibration exceeds ~10% of the nearest-neighbor distance (*49, 50*). In contrast, the remaining structural expansion of about 1.3~1.7% at $t = 1.2$ ns shows almost no dependence on excitation fluence. As discussed below, these observations reveal crucial information about dynamics of the silicon substrate and the adsorbate of interfacial ice assembly, and the energy transfer between the two.

Discussion

Understanding the dynamics of interfacial ice requires knowledge of that of the underlying substrate because water molecules have no absorption at 800 nm, and dynamical changes are initiated in the substrate. I shall first address the fluence-dependent responses of H/Si(111) upon illumination of an infrared pulse, followed by discussion about the meaning and implication of observing a structural isosbestic point. A complete picture for the dynamics of interfacial water–substrate composite, together with the time scales involved, will be presented afterward.

A. Dynamics of Hydrogen-terminated Silicon

Silicon is a semiconductor with an indirect band gap of $E_g = 1.165$ eV at $T = 100$ K (*51*). Energetically, excitation by one-photon absorption (1PA) at 800 nm ($E = 1.55$ eV) can be achieved in silicon; however, conservation of momentum requires simultaneous generation of phonon(s) in the lattice. As a result, the phonon-assisted, indirect absorption has a very low probability (i.e., a small absorption coefficient, or equivalently, a large penetration depth on the order of tens of μm) when compared with a direct absorption. In contrast, two-photon absorption (2PA) offers an excitation energy ($E = 3.10$ eV) that is close to the direct gap near the Brillouin zone center Γ ($E_0^{'} \sim 3.35$ eV) and along Λ line ($E_1 \sim 3.45$ eV) (*52*). Photoexcitation by 2PA is therefore expected to become more important as the fluence of 800-nm light increases above a certain threshold (*53*).

Previously, the structural dynamics of gallium arsenide, a direct-gap semiconductor, was discussed in a detailed study from this laboratory using UEC (Ch. 4). The important dynamical processes involved include (i) the antibonding character caused by electrons photoexcited into the conduction bands, which leads to the anisotropic lattice expansion, (ii) the cascade of transfer of the above-gap excess energy from photoexcited carriers to optical phonons, which results in the lattice motion and consequently a diffraction intensity decrease, (iii) the subsequent optical-to-acoustic phonon decay, which induces the inhomogeneity in the lattice structure and therefore diffraction width broadening, and (iv) on a longer time, carrier and energy diffusion into the bulk and other processes such as radiative and Auger recombination, which contributes the sub-nanosecond to nanosecond dynamics. These processes can also be used to describe the dynamics of the silicon substrate in this study.

With the optical-phonon energy of 64 meV at Γ (*51*) and the time constant of 240 fs for carrier–phonon scattering in silicon (*53, 54*), each photoexcited electron–hole pair by 1PA can produce up to 6 optical phonons in the lattice in less than 2 ps; each pair by 2PA, however, has much more excess energy and is able to generate up to 30 phonons in about 7 ps, as long as the effect of band filling due to Pauli exclusion principle is not severe. Therefore, once the excitation fluence is large enough, one should expect a major role of the 2PA carriers in the structural dynamics of silicon probed by UEC; after convolution with the instrumental response of 7 ps, a diffraction intensity decrease due to phonon motions is anticipated to be on a 10-ps time. This has been observed experimentally (for excitation by 266-nm light, considering its direct absorption and large excess energy to release from the carriers), as shown in the inset of Fig. 3c and early-time depletion of Fig. 4c in Ref. 55.

In this study, intensity of the specular spot from the substrate is also seen to decrease on a 10-ps time. It signifies, on such a time scale, an increase in the atomic motions near the surface that destroys the surface homogeneity (coherence) required for stronger specular reflection (Fig. 11c). Such an observation also infers the importance of 2PA in silicon to dynamics of the substrate and consequently that of the interfacial ice assembly, in the fluence range used here. From $t = 10$ ps to $t = 50$ ps, the lattice motions remain at a substantial level because of the continuing optical-phonon generation by carriers that is delayed due to the hot-phonon effect and intervalley carrier–carrier scattering (Ch. 4). Later, the decay of atomic motions is found to exhibit a fast component with a time constant of $\tau_{\text{fast}} \sim 40$ ps and a slow one on the sub-nanosecond scale.

The vital role of 2PA in silicon at early times is further evidenced by the fluence dependence of dynamical responses in the interfacial ice assembly (Fig. 13). According to Ref. 53, the highest fluence used produces mainly energetic 2PA carriers that can supply a substantial amount of energy, leading to the current observation of the large lattice expansion in ice *Ic* crystallites. At one third of this fluence or below (i.e., at ≤ 30 mJ/cm^2), however, nearly no dynamical change in ice was measurable. Based on this nonlinear response, together with the fluence-dependent dynamical portion in the diffraction profile (Fig. 13a) and the argument concerning carriers' excess energy available to structural dynamics, we reach the conclusion that the 2PA mechanism predominantly defines the dynamics of interfacial ice at early times. With such an understanding the result of Fig. 13a can therefore be explained, through a simple calculation using Gaussian profiles of the same width to represent different optical fluences on the substrate, and a cut-off threshold for the effective 2PA region within the electron-probed range (Fig. 13a, inset). The threshold is estimated to be ~25 mJ/cm^2, in a good agreement with the experimental finding and with the trend shown in Fig. 13b.

At longer times, relaxation of the silicon substrate is achieved through mechanisms such as carrier diffusion into the bulk (*56*), Auger recombination (*57*), radiative recombination, and heat diffusion (*58*). Auger recombination effectively reduces the number of carriers and releases additional energy to the lattice, which becomes the energy source at longer times. Other mechanisms effectively remove energy from the surface region and hence affect the energy content in the overlaying ice assembly. As for the Si–H vibration at the interface, previous studies showed its lifetime to be ~0.8 ns (*59*). Although such a time scale seems relevant, however, these vibrators are less important to our observations because the energy that causes structural motions is from the photocarriers and phonons that are subsequently generated; Si–H vibration plays at most the role of energy-transfer intermediate at the interface.

B. Structural Isosbestic Point

In spectroscopy, the curve crossing behavior at a common point in the spectra—known as an isosbestic point—is regarded, when relevant, as a signature of a chemical reaction or structural interconversion in progress between two species whose total concentration remains constant. In diffraction (capable of direct structure probing), however, such a behavior—naturally termed a "structural isosbestic" point—was rarely reported even in equilibrium studies (*60*) and was recently found in time-resolved experiments from this laboratory (Chs. 7 and 9). Similar to the argument in the spectroscopic counterpart, the appearance of such points in diffraction curves at transient times indicates a distinct structural conversion from the unexcited ground state to excited one(s), as these states are causally related due to the nature of the UEC technique. In fact, this conversion further signifies the phenomenon of nonequilibrium phase transformation, given the distinct difference between the two states involved and their separation by a free-energy barrier (overcome through excitation) in phase space.

Typical and expected diffraction changes in UEC are continuous profile shifts with intensity decrease and recovery, as observed in many previous studies (see, e.g., Chs. 4 and 5). In highly correlated materials, photoexcited carriers forming transient macroscopic domains lead to the two-state transformation behavior (Ch. 7). The current observation of structural isosbestic points in the dynamics of interfacial ice, similar to the result in Ch. 9, hence reflects the unusual properties of a hydrogen bond network upon an external input of vibrational energy. The observed nonequilibrium phase transformation in ice *Ic* crystallites is further confirmed by the fact that curve crossing is clearly seen for all intense diffraction rings from ice, and the conclusion of isotropic expansion based on the ring shifts is compatible with principally random orientation of ice crystallites.

Additional evidence for the existence of structural isosbestic points and the inferred phase transformation comes from the constant total intensity during curve crossing, an observation that is equivalent to the total concentration of the two species being constant during a chemical reaction or conversion in the spectroscopic counterpart. It is because the initial and final states of the conversion have the same electron diffraction cross section as both contain the same number and types of atoms. In the current study, the result of Fig. 10b therefore strengthens our picture.

It is noted that, in spectroscopic studies, the appearance of an isosbestic point in the spectra as evidence for interconverting chemical or structural species has been called into question (*61, 62*). However, the main problem there is the presence of inhomogeneous broadening. In diffraction, the well-defined Bragg spots or rings can only originate from a long-range ordered (homogeneous) structure, rather than from an ensemble or inhomogeneous distribution of distances. Moreover, the clear shifts of diffraction peaks during the early-time dynamics, with the existence of only one isosbestic point for one ring and no overlap in the wings, are in sharp contrast with the results given in Ref. 61. It is worth noting that the curve crossing behavior in the upper panels of Fig. 9 cannot be simply reproduced by adding a series of small profiles with the same width and located at different s values, thus the notion of continuous structural change is invalidated. In fact, the well-separated peaks before the time zero and after 60 ps demarcate the two distinct structures involved, each with a well-defined diffraction peak width. Furthermore, as suggested in Ref. 61, the confirmation of a true chemical or structural conversion must come from time-dependent measurements, as reported here using UEC.

C. Dynamics of Interfacial Polycrystalline Ice

Dynamics of polycrystalline ice heavily depends on that of the underlying substrate (Ch. 9). From the estimate ice film thickness, approximately 10^{14} water molecules were accumulated above the surface in the region of laser heating and electron probing. Compared with the carrier density [on the order of 10^{20} cm^{-3} (*53*)] created near the interface and the subsequent generation of phonons, the number of water molecules and their heat capacity are limited. Thus, dynamics of the silicon substrate is not much altered by the existence of interfacial ice, but dynamics of the latter follows closely that of the former.

Ice can receive energy from the underlying substrate through vibrational coupling (phonon generation) in the lattice. Cubic ice exhibits four different vibrational bands in the infrared spectrum: intramolecular O–H stretching, intramolecular H–O–H bending, librational and translational modes in decreasing order of the corresponding frequency (*63*). An efficient energy transfer is therefore expected when frequencies of the phonons

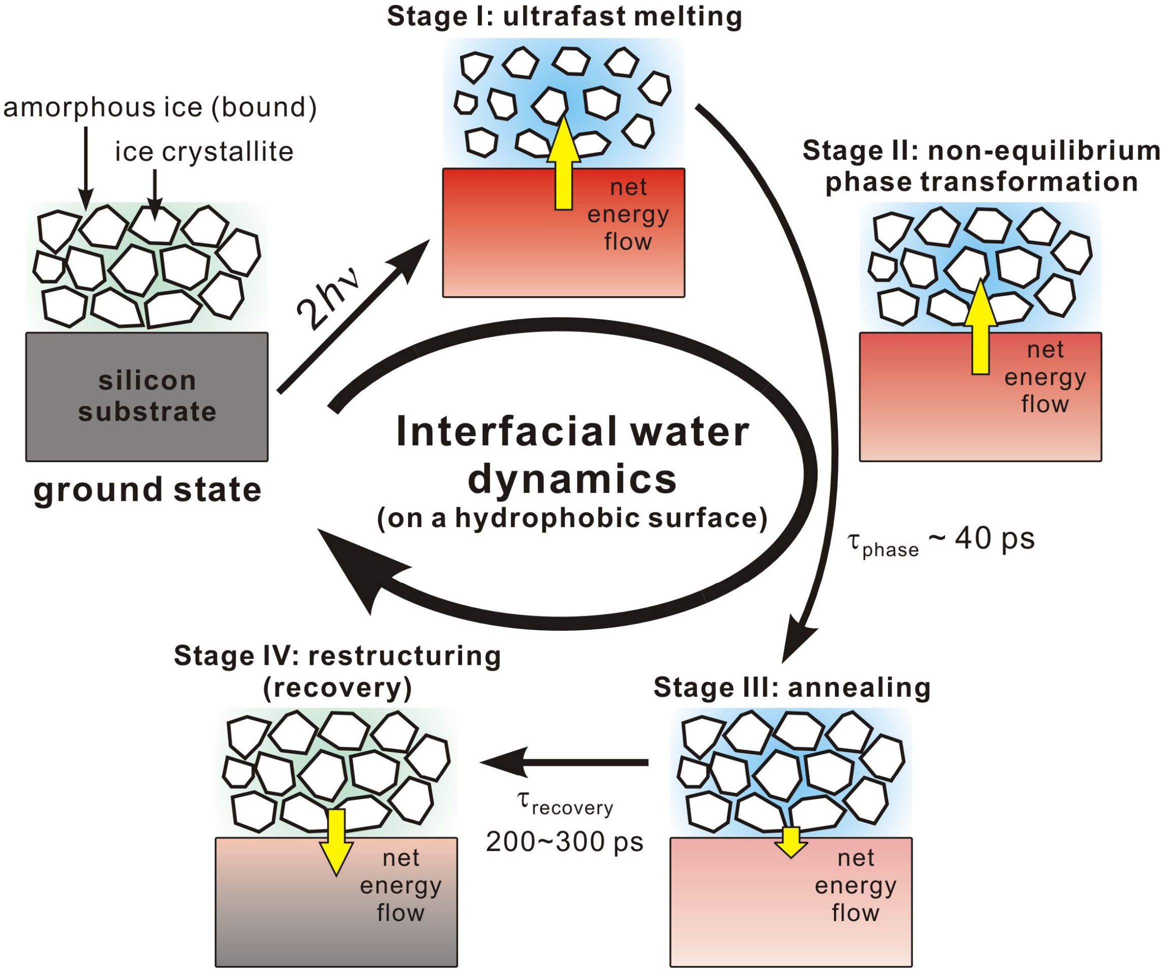

Fig. 14. Schematic representation of dynamics of the ice assembly on H/Si(111). For the substrate, the gray color and the red of different color levels represent the unexcited status and regions with different photoexcitation levels, respectively. The yellow arrows indicate the direction of the net energy flow in different stages. For interfacial ice, the different sizes of ice crystallites (not drawn to scale) are depicted to illustrate the structural dynamics at work in different stages. The sky blue (pale green) color is used to indicate water molecules that have a larger (low) mobility in the amorphous part of the ice assembly.

in silicon and in ice are matched. Optical phonons in silicon have a frequency of ~500 cm^{-1}, and acoustic ones are of even lower frequencies (*51*). Thus, excitation in the intramolecular bands of ice is unlikely because of their high frequencies, but the lower bound of the librational band and, more importantly, the entire translational vibrational band are in the frequency range of silicon phonons (*64, 65*). It is therefore not merely a coincidence to find translational movement of water molecules into an expanded structure as energy transfers from silicon to the translational vibrational band of ice. It is noted that across-interface carrier transfer (*66, 67*) from silicon to the polycrystalline ice, as an energy transfer pathway, is of little concern because of the semiconducting (nonmetallic) nature of silicon, insufficient carrier energy, and the less relevant sub-picosecond time scale involved. Such carrier transfer for the induction of a permanent structural change (*68*) can also be eliminated, since no diffraction change was accumulated in the repeated experimental cycles at 1 kHz.

With the understanding of energy transfer across the interface, the following picture emerges for the four stages of structural dynamics (Fig. 14).

C.1. Stage I—Ultrafast Melting

In the initial 20 ps after the laser heating, carriers photoexcited in silicon through 2PA start to release their excess energy preferably by generating optical phonons, which anharmonically decay [on a time scale of ~4 ps (*69*)] into acoustic phonons of lower frequencies that are able to couple with the translational vibrational band of ice *Ic* and hence transfer energy. The necessary time for this process was experimentally discernible from the small time difference between the onset of ice diffraction intensity decrease (purple in Fig. 11b) and that of silicon specular intensity drop (Fig. 11c). Upon receipt of energy into its structure, atoms in the ice *Ic* crystallites undergo enlarged vibrational motions; those near the grain boundaries may even exhibit significant translational deviation from their original positions, a transient phenomenon that can be termed ultrafast melting. This is evidenced by the initial decrease of diffraction intensity before the profile shift (Fig. 9, upper panels).

From the initial 7% and 17% intensity decrease (Fig. 10b), the induced vibrational amplitude, $\langle \delta u^2 \rangle^{1/2}$, is estimated to be about 0.27 Å and 0.44 Å, respectively, for oxygen atoms using the Debye–Waller factor (Eq. 16 of Ch. 2). These numbers are much greater than the root-mean-square displacement of at most a few hundredth of an angstrom at $T = 100$ K, and also larger than the zero-point amplitude of the oxygen atoms (*64*). Moreover, the induced motions reach about 10% and 16% of the nearest-neighbor O–O distance of 2.75 Å, which is close to or exceed the equilibrium Lindemann limit for thermal melting. However, the observed structural dynamics is not induced through thermal means, and it seems that the ice assembly withstands the vibrational motions and resists the loss of water molecules on this ultrashort time scale, suggesting connectivity and the cooperative nature of a hydrogen bond network.

Large atomic motions in the amorphous part of the ice assembly and near the crystallite boundaries are crucial and necessary for the later dynamics. Given the indefinite structure of amorphous ice and the principally random orientation of crystallites, because of orientational mismatch of vibrational modes, energy transferring across the interface will be "trapped" and retain in the assembly, instead of wavelike acoustic propagation that has been noted in the crystalline ice structure (*24*). If those atoms remained in a somewhat rigid network, ice *Ic* crystallites would encounter restraint during the later expansion because of the limited space, which hinders the accommodation of energy input in the assembly. Therefore, an increased mobility (and consequently structural flexibility) for those water molecules can be inferred.

C.2. Stage II—Nonequilibrium Phase Transformation

In this stage, generation of a significant number of phonons persists in the substrate (indicated by the sustaining reduced specular intensity shown in Fig. 10c, $t = 10$ ps to $t = 50$ ps), and energy continues to couple into the ice assembly with a small time delay (Fig. 10b, $t = 20$ ps to $t = 60$ ps). It was to our surprise to discover that ice *Ic* crystallites, supported by this "phonon bath," undergo a two-state-only structural phase transformation rather than a continuous change. We want to emphasize that this observation is not due to the resolution limit in time or in space. As shown in Fig. 11b, the new phase develops with a time constant of $\tau_{\text{phase}} \sim 40$ ps that is similar to the duration of Stage II, signifying a causal relation between the substrate dynamics and the structural transformation of interfacial ice.

The observed large expansion of ice lattice is also quite special among the laser-induced ultrafast structural dynamics. Most of the time-resolved diffraction studies [including x-ray's (*70*)] reported on the lattice change of materials that are initially photoexcited by photons directly. For interfacial ice, however, it is the *phonon* field indirectly generated underneath (from carriers) that leads to the expansion. Also, ice *Ic* crystallites were found to expand isotropically, unlike the unidirectional motion observed in a supported model membrane (*71*). The difference can be attributed to the randomness in crystallites' orientation such that the spatial asymmetry (i.e., the special role of the surface normal direction) manifested in almost all other UEC studies (see, e.g., Chs. 4, 5 and 7 and Ref. 71) no longer exists here.

It is also intriguing to find that, under a similar excitation condition, the lattice expansion of ice is much larger than that of covalently bonded systems (*71*) without sublimation, a phenomenon that may be directly associated with the relatively small strength of an individual hydrogen bond but the flexible and cooperative nature of a network (*72, 73*). The dynamical change is nonthermal in that an unreasonable temperature rise of thousands of Kelvin would be derived using the thermal expansion coefficient of ice (*74*). The fluence dependence of expansion of the new phase appears to be linear with a threshold (Fig. 13b, solid dots); however, since the dynamical portion is also dependent on fluence (Fig. 13a), it is more sensible to compare the total volume increase, which is, effectively, the product of the numbers in panels a and b of Fig. 13 at each fluence. We found from this analysis a quadratic dependence with a similar threshold, consistent with the generation of 2PA carriers being quadratically dependent on fluence, and the aforementioned dominant role of these carriers as the ultimate energy source for ice expansion.

This new dynamical property of polycrystalline ice under a strong external perturbation may be important to deeper understanding of the collective and dynamic nature of a hydrogen bond network, on a scale beyond the size of small water clusters (*75*). The different dynamics for polycrystalline and crystalline (*24*) structures are also quite intriguing, and will be detailed in another work.

C.3. Stage III—Annealing

Following the phase transformation, the diffraction intensity recovery at the transformed profile position (Fig. 9, upper panels after curve crossing) is indicative of the first step toward structural relaxation. It means a structural change in the ice assembly opposite to that during Stage I. That is, vibrational motion of atoms in the ice *Ic* crystallites becomes reduced, and those water molecules near the grain boundaries may even adopt positions that fit the adjacent crystalline order, a transient phenomenon that can be termed annealing. Consequently, the new phase becomes fully mature in this stage, and the diffraction intensity finally reaches the same value as that of the original phase (Fig. 11b, after the yellow region).

The governing factor for this structural annealing is that the energy input from the substrate starts to drop significantly in Stage III, as evidenced by the fast recovery with $\tau_{\mathrm{fast}} \sim 40$ ps shown in the inset of Fig. 11c. Now, the direction of the net energy flow is going to reverse; it was upward from the substrate to the assembly in Stages I and II (Fig. 14). Therefore, it can be reasonably concluded that, toward the end of Stage III, a dynamical equilibrium between the ice assembly and the silicon substrate is established, leading to the recovery of ice–substrate composite in the next stage.

C.4. Stage IV—Restructuring

On the sub-nanosecond to nanosecond time scale, ice *Ic* crystallites restructure by recovering continuously toward the original lattice constant (Fig. 12), along with the slow relaxation of the underlying silicon substrate. The weak dependence of the recovery time constant, τ_{recovery}, on the ice film thickness indicates that the energy dissipation in silicon into the bulk is the most important determining factor for relaxation of interfacial ice. Again, the reason is that the heat capacity of those interfacial water molecules is relatively insignificant when compared with that of the substrate, and no major bottleneck in the adsorbate–substrate heating and cooling.

It is interesting to find that the remaining lattice expansion of ice at $t = 1.2$ ns is almost fluence independent (Fig. 13b, open circles), implying a larger apparent rate for restructuring in the case with a higher fluence. These results become understandable when the status of the silicon substrate is examined. At higher fluences, the effective penetration depth for 2PA is smaller (i.e., gradient of the carrier density profile along the surface normal is larger), which leads to faster carrier and heat diffusion into the bulk. The large number of carriers by 2PA makes Auger recombination occur in a faster rate, resulting in a faster substrate relaxation. The combined effect is that the residual change at $t = 1.2$ ns in the substrate becomes less fluence dependent, and so does that of the interfacial ice.

Another intriguing observation is that the diffraction intensity remains a constant value as the original in this stage (Fig. 10b, inset), while the profile is shifting continuously (Fig. 9, lower panels). It signifies that the average atomic motion has been quenched to a level similar to that before the zero of time, although all the intermolecular distances are appreciably larger than the equilibrium values. As a result, the validity of using a Lennard–Jones type of anharmonic potential with fixed parameters to describe the fast structural dynamics of a water assembly becomes questionable, because such a model would anticipate larger intermolecular vibrations in an expanded lattice. Further theoretical endeavors are therefore encouraged to investigate whether the electrostatic term included in many water models (*76, 77*) can resolve this issue and satisfactorily explain the experimental observation here, or some modification for the intermolecular interaction term (*78, 79*) or the overall pair-wise potential (*80*) can be made. In addition, through modeling, the coupling between polarization (partial charges) of a water molecule and translational molecular movements in the network (*81*) may be revealed for transient structures that can only be accessed dynamically.

Concluding Remarks: Interfacial Ice on H/Si(111) and on Graphite

From UEC studies of an assembly on different hydrophobic surfaces (Ch. 9), we are able to gain further insights on the structural and dynamical properties of interfacial ice. Statically, due to their weak interaction with the substrate, water molecules do not adopt the symmetry of the substrate surface and the azimuthal orientations of ice crystallites are therefore random. However, the terraced surface morphology of highly oriented pyrolytic graphite provides an additional guiding force to assist the order of water layers along the surface normal direction. In the present study, the lack of such a template structure on H/Si(111) makes the intermolecular water–water interaction the most dominant factor for crystallites' orientation, resulting in a diffraction pattern of rings instead of observation of well-defined Bragg spots.

From analysis of the diffraction patterns the structure of polycrystalline ice was confirmed to be of the cubic form, ice *Ic*. Further away from the substrate, because of the energetics at the ice–vacuum interface, ice *Ic* crystallites prefer the exposure of {110} planes to minimize the number of dangling O–H bonds, leading to the observation of {110} preferred orientation for ice crystallites near the vacuum in a thick assembly. Structural optimization with consideration of this preferred orientation gave a lattice constant that agrees well with the literature value.

For the dynamics of interfacial ice, we found the determining factor to be the dynamics of the substrate following an ultrafast "*T*-jump" by a femtosecond infrared pulse. Carriers photogenerated in silicon by two-photon absorption were the most crucial source of energy because of their larger above-gap excess energy available to the lattice. The across-interface energy transfer from the substrate couples with the translational vibrational band of ice and causes initial large atomic motions, or a melting-like phenomenon, in the ice assembly, as manifested by an initial diffraction intensity decrease on an ultrashort time scale. Subsequently, nonequilibrium phase transformation of ice *Ic* crystallites into an isotropically expanded lattice follows, which is evidenced by the appearance of structural isosbestic points, a curve crossing behavior, in the temporal evolution of diffraction profiles.

As soon as the substrate experiences a significant reduction in its lattice energy, the ice assembly starts its path to restructuring, first by greatly quenching the atomic motions or by structural annealing, which is inferred from the quick recovery of diffraction intensity to the original level. At longer times, the substrate undergoes a slow relaxation, and the expanded ice crystallites exhibit a continuous decrease in their lattice constant, toward the equilibrium value. Based on the peculiar evolution of the observed diffraction changes, theoretical investigations are suggested in order to acquire better understanding about the correlation between molecular polarization and intermolecular interaction at transient times.

It was shown that, although the aforementioned picture for the four stages of ice structural dynamics remains robust, the dynamical behaviors of interfacial ice at different stages and their corresponding time constants are closely related to the characteristics of substrate dynamics. Graphite was found to exhibit ultrafast structural contraction and expansion (*82*), and it is therefore understandable to see that the interfacial ice on graphite goes through the first three stages of structural dynamics more quickly than that on silicon does (Ch. 9). Also, graphite is a semimetal that has no band gap and adsorbs 800-nm light better, which makes the photocarriers more concentrated and their energy entirely available to the lattice dynamics. The much larger expansion of the ice assembly on graphite is thus expected. However, regardless of what the substrate is, the large atomic motions and significant expansion of ice at transient times do not lead to a total melting or sublimation of the assembly. This picture was consistently suggested by a previous spectroscopic study of interfacial D_2O ice, using sum-frequency generation with longer time resolution, although neither the structure nor the order can be directly observed with atomic resolutions (*21*).

The observations made by ultrafast electron crystallography unravel the unique nature of structure and dynamics of interfacial water assembly on hydrophobic substrates. It may be interesting to find some similarity in time constants reported in a study of the structural dynamics of liquid water following direct electronic excitation, using time-resolved x-ray diffraction with a poor temporal resolution (*83*). With these recent developments of ultrafast diffraction methods, we are now equipped with direct means for elucidating structures and dynamics at nanometer scale, such as those during phase transformations (*29, 30, 84*) or concerning hydrophobic/hydrophilic properties at interfaces (*85-87*) and their contrast with bulk ones (*88*).

References and Footnotes:

1. G. M. Whitesides, B. Grzybowski, *Science* **295**, 2418 (2002).
2. K. B. Eisenthal, *Chem. Rev.* **96**, 1343 (1996).
3. G. A. Jeffrey, *An introduction to hydrogen bonding* (Oxford Univ. Press, New York, 1997).
4. M. Binggeli, C. M. Mate, *Appl. Phys. Lett.* **65**, 415 (1994).
5. M. A. Henderson, *Surf. Sci. Rep.* **46**, 5 (2002).
6. A. Verdaguer, G. M. Sacha, H. Bluhm, M. Salmeron, *Chem. Rev.* **106**, 1478 (2006).
7. K. Gawrisch *et al.*, *Biophys. J.* **61**, 1213 (1992).
8. W. Zhao, D. E. Moilanen, E. E. Fenn, M. D. Fayer, *J. Am. Chem. Soc.* **130**, 13927 (2008).
9. L. Y. Zhang *et al.*, *Proc. Natl. Acad. Sci. USA* **104**, 18461 (2007).

10. G. E. Brown *et al.*, *Chem. Rev.* **99**, 77 (1999).

11. G. E. Brown, *Science* **294**, 67 (2001).

12. S. K. Pal, A. H. Zewail, *Chem. Rev.* **104**, 2099 (2004).

13. G. M. Whitesides, P. W. Snyder, D. T. Moustakas, K. A. Mirica, in *Physical biology: from atoms to medicine,* A. H. Zewail, Ed. (Imperial College Press, London, 2008), pp. 189-215.

14. Y. Levy, J. N. Onuchic, *Annu. Rev. Biophys. Biomol. Struct.* **35**, 389 (2006).

15. G. W. Robinson, S.-B. Zhu, S. Singh, M. W. Evans, *Water in biology, chemistry and physics: Experimental overviews and computational methodologies* (World Scientific, New Jersey, 1996).

16. C. A. Angell, *Annu. Rev. Phys. Chem.* **55**, 559 (2004).

17. M. R. Yalamanchili, A. A. Atia, J. D. Miller, *Langmuir* **12**, 4176 (1996).

18. Y. R. Shen, *Nature* **337**, 519 (1989).

19. Y. R. Shen, V. Ostroverkhov, *Chem. Rev.* **106**, 1140 (2006).

20. X. C. Su, L. Lianos, Y. R. Shen, G. A. Somorjai, *Phys. Rev. Lett.* **80**, 1533 (1998).

21. J. Kubota, A. Wada, S. S. Kano, K. Domen, *Chem. Phys. Lett.* **377**, 217 (2003).

22. K. Thürmer, N. C. Bartelt, *Phys. Rev. B* **77**, 195425 (2008).

23. X. Zou, S. Hovmöller, *Acta Crystallogr. Sect. A* **64**, 149 (2008).

24. C.-Y. Ruan, V. A. Lobastov, F. Vigliotti, S. Chen, A. H. Zewail, *Science* **304**, 80 (2004).

25. W. Kern, *Handbook of semiconductor wafer cleaning technology : science, technology, and applications* (Noyes Publications, Park Ridge, N.J., 1993).

26. G. S. Higashi, Y. J. Chabal, G. W. Trucks, K. Raghavachari, *Appl. Phys. Lett.* **56**, 656 (1990).

27. P. Dumas, Y. J. Chabal, P. Jakob, *Surf. Sci.* **269**, 867 (1992).
28. P. Baum, A. H. Zewail, *Proc. Natl. Acad. Sci. USA* **103**, 16105 (2006).
29. P. Jenniskens, D. F. Blake, *Science* **265**, 753 (1994).
30. P. Jenniskens, D. F. Blake, *Astrophys. J.* **473**, 1104 (1996).
31. B. J. Murray, D. A. Knopf, A. K. Bertram, *Nature* **434**, 202 (2005).
32. B. K. Vaĭnshteĭn, *Structure analysis by electron diffraction* (Pergamon Press, Oxford, 1964).
33. Z. L. Wang, *Elastic and inelastic scattering in electron diffraction and imaging* (Plenum Press, New York, 1995).
34. I. Kohl, E. Mayer, A. Hallbrucker, *Phys. Chem. Chem. Phys.* **2**, 1579 (2000).
35. We found that it is equally effective to use a Lorentzian or polynomial function for the decay part, and the result is practically the same.
36. W. F. Kuhs, D. V. Bliss, J. L. Finney, *J. Phys. Colloq. C1* **48**, 631 (1987).
37. W. H. Barnes, *Proc. R. Soc. London Ser. A* **125**, 670 (1929).
38. W. F. Kuhs, M. S. Lehmann, *J. Phys. Chem.* **87**, 4312 (1983).
39. Diffraction profiles were calculated using kinematic scattering theory. The estimated size of ice *Ic* crystallites that were vapor-deposited on a hydrophobic surface was on the order of <100 Å. According to Ref. 32, dynamic effects would become important only when the scattering domain size is approximately 450 Å. The use of kinematic, rather than dynamic, scattering theory is therefore justified in the present work.
40. L. G. Dowell, A. P. Rinfret, *Nature* **188**, 1144 (1960).
41. L. S. Bartell, J. F. Huang, *J. Phys. Chem.* **98**, 7455 (1994).
42. G. P. Johari, *J. Chem. Phys.* **122**, 194504 (2005).

43. H. M. Rietveld, *J. Appl. Cryst.* **2**, 65 (1969).

44. T. Roisnel, J. Rodríguez-Carvajal, in *Materials Science Forum, Proceedings of the Seventh European Powder Diffraction Conference (EPDIC 7),* R. Delhez, E. J. Mittenmeijer, Eds. (2000), pp. 118-123.

45. J. Rodríguez-Carvajal, in *IUCr Commission on Powder Diffraction Newsletter*. (2001), vol. 26, pp. 12-19.

46. Least-squares refinement was performed using the program FullProf (*44, 45*). Relative atomic positions in a unit cell were of the cubic structure, and the isotropic atomic displacement factors [$B_O = 1.56$ Å^2 and $B_H = 2.02$ Å^2 (*38*)] were fixed. The diffraction peaks were described by pseudo-Voigt functions, whereas the background was modeled by a polynomial function. The cubic unit-cell parameter that determines the positions of diffraction peaks was refined during the process.

47. R. A. Young, Ed., *The rietveld method* (Oxford Univ. Press, Oxford, 1995).

48. From the aforementioned structural analysis and Figure 5, the wing regions of the (111) ring have diffraction contributions from both randomly oriented and preferentially oriented ice crystallites, whereas the central region is from the former type only.

49. J. N. Shapiro, *Phys. Rev. B* **1**, 3982 (1970).

50. J. M. Ziman, *Principles of the theory of solids* (Cambridge Univ. Press, Cambridge, 2nd ed., 1972).

51. A. Dargys, J. Kundrotas, *Handbook on physical properties of Ge, Si, GaAs and InP* (Science and Encyclopedia Publishers, Vilnius, 1994).

52. P. Lautenschlager, M. Garriga, L. Viña, M. Cardona, *Phys. Rev. B* **36**, 4821 (1987).

53. T. Sjodin, H. Petek, H.-L. Dai, *Phys. Rev. Lett.* **81**, 5664 (1998).

54. A. J. Sabbah, D. M. Riffe, *Phys. Rev. B* **66**, 165217 (2002).

55. C.-Y. Ruan, F. Vigliotti, V. A. Lobastov, S. Chen, A. H. Zewail, *Proc. Natl. Acad. Sci. USA* **101**, 1123 (2004).

56. C. V. Shank, R. Yen, C. Hirlimann, *Phys. Rev. Lett.* **50**, 454 (1983).

57. M. C. Downer, C. V. Shank, *Phys. Rev. Lett.* **56**, 761 (1986).

58. J. H. Bechtel, *J. Appl. Phys.* **46**, 1585 (1975).

59. P. Guyot-Sionnest, P. Dumas, Y. J. Chabal, G. S. Higashi, *Phys. Rev. Lett.* **64**, 2156 (1990).

60. G. W. Robinson, C. H. Cho, J. Urquidi, *J. Chem. Phys.* **111**, 698 (1999).

61. P. L. Geissler, *J. Am. Chem. Soc.* **127**, 14930 (2005).

62. J. D. Smith *et al.*, *Proc. Natl. Acad. Sci. USA* **102**, 14171 (2005).

63. C. Y. Lee, D. Vanderbilt, K. Laasonen, R. Car, M. Parrinello, *Phys. Rev. B* **47**, 4863 (1993).

64. J. E. Bertie, E. Whalley, *J. Chem. Phys.* **46**, 1271 (1967).

65. D. D. Klug, E. Whalley, E. C. Svensson, J. H. Root, V. F. Sears, *Phys. Rev. B* **44**, 841 (1991).

66. C. Gahl, U. Bovensiepen, C. Frischkorn, M. Wolf, *Phys. Rev. Lett.* **89**, 107402 (2002).

67. J. Stähler, C. Gahl, U. Bovensiepen, M. Wolf, *J. Phys. Chem. B* **110**, 9637 (2006).

68. D. Chakarov, B. Kasemo, *Phys. Rev. Lett.* **81**, 5181 (1998).

69. J. Menéndez, M. Cardona, *Phys. Rev. B* **29**, 2051 (1984).

70. M. Bargheer, N. Zhavoronkov, M. Woerner, T. Elsaesser, *ChemPhysChem* **7**, 783 (2006).

71. M. T. Seidel, S. Y. Chen, A. H. Zewail, *J. Phys. Chem. C* **111**, 4920 (2007).

72. M. I. Heggie, C. D. Latham, S. C. P. Maynard, R. Jones, *Chem. Phys. Lett.* **249**, 485 (1996).

73. P. L. Silvestrelli, M. Parrinello, *J. Chem. Phys.* **111**, 3572 (1999).

74. H. Tanaka, *J. Chem. Phys.* **108**, 4887 (1998).

75. F. N. Keutsch, R. J. Saykally, *Proc. Natl. Acad. Soc. USA* **98**, 10533 (2001).

76. W. L. Jorgensen, J. Chandrasekhar, J. D. Madura, R. W. Impey, M. L. Klein, *J. Chem. Phys.* **79**, 926 (1983).

77. H. J. C. Berendsen, J. R. Grigera, T. P. Straatsma, *J. Phys. Chem.* **91**, 6269 (1987).

78. O. Mishima, H. E. Stanley, *Nature* **396**, 329 (1998).

79. R. Kumar, J. L. Skinner, *J. Phys. Chem. B* **112**, 8311 (2008).

80. B. Guillot, Y. Guissani, *J. Chem. Phys.* **114**, 6720 (2001).

81. B. Chen, J. H. Xing, J. I. Siepmann, *J. Phys. Chem B.* **104**, 2391 (2000).

82. F. Carbone, P. Baum, P. Rudolf, A. H. Zewail, *Phys. Rev. Lett.* **100**, 035501 (2008).

83. A. M. Lindenberg *et al.*, *J. Chem. Phys.* **122**, 204507 (2005).

84. L. Delzeit, D. F. Blake, *J. Geophys. Res.* **106**, 33371 (2001).

85. B. J. Gertner, J. T. Hynes, *Science* **271**, 1563 (1996).

86. A. P. Willard, D. Chandler, *J. Phys. Chem. B* **112**, 6187 (2008).

87. P. Ball, *Chem. Rev.* **108**, 74 (2008).

88. A. D. Buckingham, J. E. Del Bene, S. A. C. McDowell, *Chem. Phys. Lett.* **463**, 1 (2008).